Chemistry of a polluted cloudy boundary layer

Citation
Jacob, Daniel J., Elaine W. Gottlieb, and Michael J. Prather. 1989. "Chemistry of a Polluted Cloudy Boundary Layer." Journal of Geophysical Research 94 (D10): 12975. doi:10.1029/jd094id10p12975.

Published Version
doi:10.1029/JD094iD10p12975

Permanent link
http://nrs.harvard.edu/urn-3:HUL.InstRepos:33490981

Terms of Use

Share Your Story

The Harvard community has made this article openly available.
Please share how this access benefits you. Submit a story .

Accessibility

Chemistry of a Polluted Cloudy Boundary Layer

DANIEL J. JACOB AND ELAINE. W. GOTTLIEB

Department of Earth and Planetary Sciences and Division of Applied Sciences
Harvard University, Cambridge, Massachusetts

MICHAEL J. PRATHER

NASA Goddard Institute of Space Studies, New York, New York

A one-dimensional photochemical model for cloud-topped boundary layers is developed which includes detailed descriptions of gas-phase and aqueous-phase chemistry, and of the radiation field in and below cloud. The model is used to interpret the accumulation of pollutants observed over Bakersfield, California, during a wintertime stagnation episode with low stratus. The main features of the observations are well simulated; in particular, sulfate accumulates progressively over the course of the episode due to sustained aqueous-phase oxidation of SO_2 in the stratus cloud. The major source of sulfate is the reaction $S(IV) + Fe(III)$, provided that this reaction proceeds by a non radical mechanism in which $Fe(III)$ is not reduced. A radical mechanism with SO_3^- and $Fe(II)$ as immediate products would quench sulfate production because of depletion of $Fe(III)$. The model results suggest that the non radical mechanism is more consistent with observations, although this result follows from the absence of a rapid $Fe(II)$ oxidation pathway in the model. Even with the non-radical mechanism, most of the soluble iron is present as $Fe(II)$ because $Fe(III)$ is rapidly reduced by O_2^-. The $S(IV) + Fe(III)$ reaction provides the principal source of H_2O_2 in the model; photochemical production of H_2O_2 from HO_2 or $O_2(-I)$ is slow because HO_2 is depleted by high levels of NO_x. The aqueous-phase reaction $S(IV) + OH$ initiates a radical-assisted $S(IV)$ oxidation chain but we find that the chain is not propagated due to efficient termination by $SO_4^- + Cl^-$ followed by $Cl + H_2O$. A major uncertainty attached to that result is that the reactivities of $S(IV)$-carbonyl adducts with radical oxidants are unknown. The chain could be efficiently propagated, with high sulfate yields, if the $S(IV)$-carbonyl adducts were involved in chain propagation. A remarkable feature of the observations, which is well reproduced by the model, is the close balance between total atmospheric concentrations of acids and bases. We argue that this balance reflects the control of sulfate production by NH_3, which follows from the pH dependence of the $S(IV) + Fe(III)$ reaction. Such a balance should be a general characteristic of polluted environments where aqueous-phase oxidation of SO_2 is the main source of acidity. At night, the acidity of the cloud approaches a steady state between NH_3 emissions and H_2SO_4 production by the $S(IV) + Fe(III)$ reaction. A steady state analysis suggests that $[H^+]$ at night should be proportional to $(E_{SO2}/E_{NH3})^{1/2}$ where E_{SO2} and E_{NH3} are emission rates of SO_2 and NH_3, respectively. From this analysis it appears that cloud water pH values below 3 are unlikely to occur in the Bakersfield atmosphere during the nighttime hours. Very high acidities could, however, be achieved in the daytime because of photochemical acid production by the gas-phase reactions $NO_2 + OH$ and $SO_2 + OH$.

1. INTRODUCTION

This paper describes an attempt to simulate the chemical evolution of the atmosphere over Bakersfield, California, during an extended wintertime stagnation episode with low stratus. We focus our attention on the oxidation of SO_2 to sulfate, and on the concomitant production of acidity. The city of Bakersfield experiences severe sulfate pollution in winter; sulfate aerosol concentrations as high as 1600 neq m^{-3} (24-hour average) have been measured [*Duckworth and Crowe*, 1979]. Bakersfield is located at the southern end of the San Joaquin Valley, in a region of major oil recovery operations which emit large amounts of SO_2. The ventilation of the San Joaquin Valley is often restricted in the wintertime because of a strong subsidence inversion based a few hundred meters above the valley floor. Such high-inversion stagnation episodes can persist uninterrupted for a week or more and are usually accompanied by extensive fog or stratus [*Holets and Swanson*, 1981].

The restricted ventilation and the presence of large amounts of suspended liquid water provide favorable conditions for observing the oxidation of locally emitted SO_2 to sulfate. *Jacob et al.* [1986]

(hereafter referred to as JMWH) made extensive measurements of aerosol composition at a network of sites in the San Joaquin Valley during a stagnation episode which lasted from January 3 to 7, 1984. They observed a progressive accumulation of sulfate aerosol over the period January 3-5 when the valley was capped by a persistent stratus deck. Sulfate concentrations decreased on January 6 following widespread fog, presumably because of fog deposition [*Waldman et al.*, 1987]. Throughout the episode, a close balance was observed between high atmospheric concentrations of acids (mainly H_2SO_4 and HNO_3) and bases (mainly NH_3). This balance was found to be a general characteristic of stagnation episodes in the southern San Joaquin Valley [*Munger et al.*, 1983; *Jacob et al.*, 1984].

We will address in this paper two major questions raised by the Bakersfield data of JMWH: (1) What were the mechanisms of sulfate production? (2) Why did the concentrations of acids and bases remain in close balance at all times?

There is considerable evidence that oxidation of SO_2 to sulfate is enhanced in cloud compared to clear air due to aqueous-phase reactions of dissolved SO_2. Aqueous-phase oxidation of SO_2 by H_2O_2 is particularly rapid; *Daum et al.* [1984] observed that H_2O_2 and SO_2 are mutually exclusive in clouds, suggesting rapid titration. Tropospheric concentrations of H_2O_2 are of the order of 1 ppb [*Logan et al.*, 1981; *Heikes et al.*, 1987]. In polluted environments such as Bakersfield the concentrations of SO_2 are usually

TABLE 1. Nomenclature of species

Nomenclature	Species
S(VI)	$H_2SO_4(aq) + HSO_4^- + SO_4^{2-} + FeSO_4^+$
S(IV)	$SO_2(aq) + HSO_3^- + SO_3^{2-} + FeSO_3^+ + HMS + HAMS + GMBS$ $+ (2x)GDBS$
N(V)	$HNO_3(g) + HNO_3(aq) + NO_3^-$
N(-III)	$NH_3(g) + NH_3(aq) + NH_4^+$
Fe(II)	$Fe^{2+} + Fe(OH)^+$
Fe(III)$_{aq}$	$Fe^{3+} + Fe(OH)^{2+} + Fe(OH)_2^+ + FeSO_3^+ + FeHOSO_3 + FeSO_4^+$
Fe(III)	$Fe(III)_{aq} + Fe(OH)_3$
Mn(II)	Mn^{2+}
Mn(III)	$Mn^{3+} + Mn(OH)^{2+}$
Cu(I)	Cu^+
Cu(II)	Cu^{2+}
$O_2(-I)$	$HO_2(aq) + O_2^-$
GLYXA	$CHOCHO(aq) + CHOCH(OH)_2 + CH(OH)_2CH(OH)_2$
MGLYA	$CH_3COCHO(aq) + CH_3COCH(OH)_2$
HMS	$H_2C(OH)SO_3^-$
HAMS	$CH_3COCH(OH)SO_3^-$
GMBS	$CH(OH)_2CH(OH)SO_3^-$
GDBS	$CH(OH)SO_3^- CH(OH)SO_3^-$

much higher, so that the oxidation of SO_2 by H_2O_2 is limited by the rate of H_2O_2 production. *Chameides and Davis* [1982] suggested that vigorous H_2O_2 production could take place in cloud droplets by the aqueous-phase reaction $HO_2 + O_2^-$. On the basis of this reaction, *McElroy* [1986a] computed H_2O_2 production rates of the order of 0.1 ppb h^{-1} for wintertime clouds over Great Britain. *Graedel et al.* [1986] argued that another mechanism for H_2O_2 production in clouds could be the aqueous-phase reduction of HO_2 and O_2^- by transition metal ions. We will see, however, that these sources are not significant under the conditions found in Bakersfield because HO_2 concentrations are very low. Entrainment of air from aloft provides a source of H_2O_2 to the boundary layer [*Gervat et al.*, 1988], but this source should be small in our case since the residence time of air in the Joaquin Valley during stagnation episodes is of the order of several days [*Reible*, 1982; JMWH]. The fact that SO_2 oxidation was observed in the JMWH study suggests either that SO_2 oxidants other than H_2O_2 dominated sulfate production or that H_2O_2 was produced rapidly by a mechanism not recognized in previous chemical models.

We will show in this paper that the Fe(III)-catalyzed autoxidation of S(IV) can explain most of the sulfate production observed in the JMWH study, as well as the close balance between acids and bases. The importance of transition metal ions as aqueous-phase SO_2 oxidants in polluted environments has been hypothesized in several model papers [*Jacob and Hoffmann*, 1983; *Seigneur and Saxena*, 1984; *Graedel et al.*, 1986]. *Jacob and Hoffmann* [1983] argued that the Fe(III)- and Mn(II)-catalyzed autoxidation of S(IV) could provide the major source of sulfate in urban nighttime fogs. Recent kinetic work suggests that these processes may be even more important than previously calculated in the models. *Martin and Hill* [1987a,b] found that the rate constants previously reported for the S(IV) + Fe(III) and S(IV) + Mn(II) reactions underestimate several times the values to be expected in clouds because of the strong dependence of the rate constant on ionic strength. *Conklin and Hoffmann* [1988a] proposed a non-radical mechanism for the S(IV) + Fe(III) reaction in which Fe(III) acts as a catalyst for the autoxidation of S(IV); this mechanism yields H_2O_2 as a reaction product, effectively doubling the yield of sulfate. However, *Martin* [1988] argued that the

S(IV) + Fe(III) reaction proceeds by a radical mechanism with Fe(II) and SO_3^- as immediate products. We will see that the choice of mechanism has a major effect on the predicted sulfate concentrations.

Another significant source of sulfate is the oxidation of SO_2 by OH, both in the gas phase and in the aqueous phase. The aqueous-phase reaction S(IV) + OH produces SO_3^- and initiates a S(IV) oxidation chain propagated by oxidation of SO_3^- to SO_5^- and reactions of the successive radical intermediates SO_5^-, SO_4^-, and Cl_2^- with S(IV) [*McElroy*, 1986b]. Recent kinetic studies have increased considerably our understanding of the propagation reactions involving HSO_3^- and SO_3^{2-} as the reactive S(IV) species [*Huie and Neta*, 1984, 1987; *McElroy*, 1988; *Wine et al.*, 1989]. However, in polluted clouds, S(IV) is mainly present as S(IV)-carbonyl adducts [*Munger et al.*, 1986], whose reactivities with the above radicals are unknown. The importance of the aqueous-phase reaction S(IV) + OH as an atmospheric source of sulfate depends in a crucial measure on the participation of S(IV)-carbonyl adducts in the chain initiation, propagation, and termination steps. The main features of this dependence will be outlined here.

Our discussion will be based on a one-dimensional photochemical model which includes comprehensive descriptions of gas-phase and aqueous-phase chemical processes, and detailed computation of radiation intensities in and below cloud. The model is used to simulate the chemical evolution of the atmosphere over Bakersfield during the January 3-5, 1984, stagnation episode documented by JMWH. Throughout that episode the boundary layer was capped by a strong inversion based at approximately 400 m above ground level (AGL), and a nonprecipitating stratus cloud occupied the upper part of the boundary layer below the inversion. We describe the model in section 2 (the solution to the equation of radiative transfer for the cloudy atmosphere is presented in the appendix). Section 3 gives an overview of model results focusing on comparisons with observations. The different aqueous-phase S(IV) oxidation mechanisms contributing to sulfate production are analyzed in section 4. Sensitivity calculations are discussed in section 5 and demonstrate that sulfate production in the model is controlled by the availability of NH_3, thus explaining the close
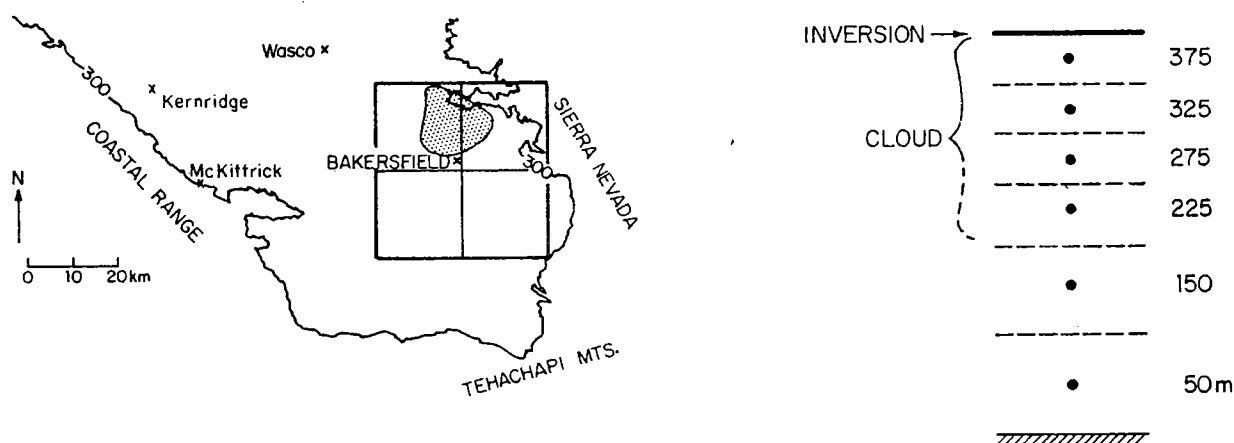
Fig. 1. The San Joaquin Valley of California: model domain and one-dimensional vertical grid. The 300-m contour (altitude above sea level) delineates the edge of the valley. The model domain (thick line) consists of the four NAPAP 5.2 grid boxes (thin lines) encompassing Bakersfield and the surrounding area. The shaded area outlines the region of maximum SO_2 emissions (0.3-0.6 tons km^{-2} d^{-1} [Aerovironment, Inc., 1984]. The vertical structure of the boundary layer is resolved with six layers extending from the ground to the inversion base (400 m above ground level). Layers 4-6 are cloudy at all times; layer 3 is cloudy at night but clear in the daytime.

balance observed in the field between total concentrations of acids and bases. The sensitivity of cloud water pH to changes in emissions is discussed in light of this result. Concluding remarks are in section 6.

2. MODEL DESCRIPTION

The transport of pollutants is simulated with a one-dimensional dynamical model for the cloud-topped boundary layer. Gas-phase chemistry is modeled with the detailed photochemical smog mechanism of Lurmann et al. [1986], and aqueous-phase chemistry is modeled with an updated version of the Jacob [1986] mechanism. The radiation intensities in and below cloud are computed by solution to the equation of radiative transfer for a Mie-scattering plane-parallel atmosphere. Computation of gas-droplet transfer fluxes accounts for gas-phase, interfacial, and aqueous-phase resistances to mass transport [Schwartz and Freiberg, 1981; Jacob, 1986]. In this section we discuss the original and case-specific components of the model. Detailed discussions of the gas-phase chemistry and gas-droplet transfer components can be found in the original references.

Many chemical species of importance to the simulation are rapidly exchanged between the gas phase, the cloud droplets, and the below-cloud aerosol. To facilitate the presentation we make extensive use of a nomenclature based on oxidation states (Table 1). The nomenclature also includes abbreviations for some of the organic aqueous-phase species. We define [A] as the concentration of constituent A per unit volume of cloud water, and (A) as the concentration of A per unit volume of air. Cloud water concentrations are given in units of M (moles per liter of water), aerosol concentrations in units of moles m^{-3} or eq m^{-3} (moles or equivalents per cubic meter of air), and gas-phase concentrations in units of mixing ratio (volume per volume) or molecules per cubic centimeter. Air densities in the model range from 2.53×10^{19} to 2.62×10^{19} molecules cm^{-3} depending on altitude and time of day.

2.1. Dynamical Model

The vertical structure of the boundary layer is resolved with six layers extending from the valley floor to the inversion base, which

is located at a constant altitude of 400 m AGL and which constitutes the upper boundary of the model domain (Figure 1). The dew point is fixed at 7°C, and layer 1 temperatures are assumed to range from 8°C (night) to 9°C (day), on the basis of observations from the Bakersfield National Weather Service station [National Climatic Data Center, 1984]. Temperatures in the upper layers are calculated from the adiabatic cooling rate; when saturation is reached, the excess water vapor condenses to form a non precipitating cloud (Figure 2). The cloud thicknesses and liquid water contents computed in this manner are consistent with the observations of JMWH.

Vertical transport within the cloud-topped boundary layer is simulated as an eddy diffusion process, which should be a reasonable approximation since updraft velocities in stratus clouds are relatively low. A constant and uniform eddy diffusion coefficient $K_z = 1 \times 10^5$ cm^2 s^{-1} is assumed [Roach et al., 1982; Caughey et al., 1982]. The entrainment velocity at cloud top is fixed at $V_e = 0.2$ cm s^{-1} in order to provide a boundary layer residence time (2.3 days) consistent with the observed time constant for accumulation of CO at the Kernridge site on the west side of the valley
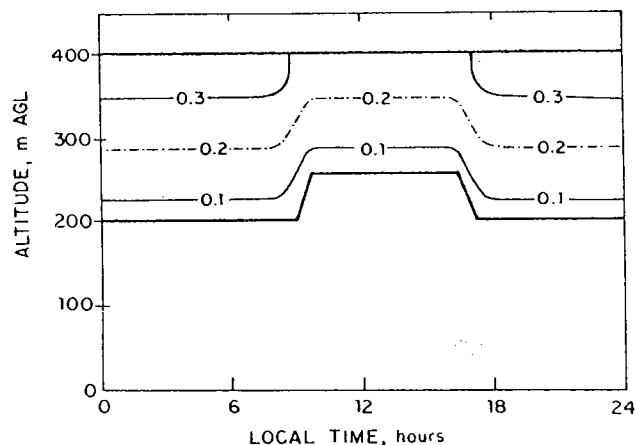

Fig. 2. Simulated cloud liquid water content (grams per cubic meter) as a function of altitude and time of day. The thick line is the cloud boundary.

TABLE 2. Initial and Upper Boundary Conditions

	Initial	Upper Boundary	Notes
		$neq\ m^{-3}$	
S(VI)	226	10	a
N(V)	371	25	a
N(-III)	545	25	a
		$nmoles\ m^{-3}$	
Fe	0.45		b
Mn	0.033		b
Cu	0.017		b
Cl⁻	25		b
Na⁺	25		b
		ppb	
O_3	5	20	c
CO	250	200	c
NO_x	20	0.1	c
SO_2	1	0.1	c

Notes: *a*, Initial concentrations are taken from measurements at Bakersfield on January 3 at 0000-0400 local time (JMWH). Upper boundary concentrations are taken from measurements at mountain sites above the valley (JMWH). *b*, Concentrations are held fixed throughout the simulation at their initial values, which are taken from the mean fog water concentrations observed in Bakersfield during the January 1984 experiment scaled by the liquid water content (JMWH). The values shown in the table are total atmospheric concentrations; in the case of trace metals, we assume that the soluble fraction represents 30% of this total. The initial partitioning of Fe, Mn, and Cu between oxidation states is 50/50 for Fe(II)/Fe(III), 10/90 for Cu(I)/Cu(II), and 600/1 for Mn(II)/Mn(III). This partitioning evolves over the course of the simulation as a result of aqueous-phase reactions. *c*, Initial concentrations are taken from measurements at Kernridge on January 3 at 0000 local standard time (JMWH). Upper boundary conditions are typical regional background concentrations.

(JMWH). Such an entrainment velocity is within the range observed in stratus clouds [*Roach et al.*, 1982]. The air entrained into the boundary layer from the top is assumed to contain background pollutant concentrations, taken when available from measurements at mountain sites above the valley (Table 2). Deposition velocities are fixed at 1 cm s⁻¹ for all oxidants (e.g., O_3, NO_2, PAN) and water-soluble gases (e.g., HNO_3, NH_3, SO_2, RCOOH, RCHO, ROOH), and at 0.1 cm s⁻¹ for (SO_4^{2-}, NO_3^-, $S(IV)^-$, NH_4^+) aerosol [*Walcek et al.*, 1987]. Other species (e.g., NO, alkanes, alkenes) are not removed by deposition.

The model domain is a 40 km x 40 km region defined by the four National Acid Precipitation Assessment Program (NAPAP) grid boxes encompassing Bakersfield and the immediately surrounding area (Figure 1). The domain is assumed to be well mixed horizontally and not ventilated by advection. The assumption of horizontal mixing has some justification since horizontal transport in the valley during stagnation episodes is contributed mostly by small-scale eddies and katabatic flows near the mountain slopes, which are diffusive rather than advective on a 40-km spatial scale [*Reible*, 1982]. The size of the model domain accounts for appropriate horizontal diffusion of pollutants emitted from the city of Bakersfield and from the oil fields immediately to

the north; it excludes the town of Wasco where measured aerosol concentrations during the stagnation episode were significantly lower than at Bakersfield (JMWH).

Pollutant emissions are taken from the NAPAP 5.2 1980 hourly emission inventory for a winter weekday [*Environmental Protection Agency*, 1986], averaged over the four grid boxes of the model domain. The January 3-5, 1984 episode extended from a Tuesday to a Thursday, i.e., over weekdays only; therefore we assume that pollutant emissions did not vary from day to day. The 24-hour average emission rates for NO_x, nonmethane hydrocarbons, and CO are 5.7×10^{11} molecules cm⁻² s⁻¹, 1.6×10^{12} molecules C cm⁻² s⁻¹, and 1.9×10^{12} molecules cm⁻² s⁻¹, respectively. Modified emission rates are used for SO_2, NH_3, and organic acids. For SO_2 we assume a constant emission rate of 6.7×10^{11} molecules cm⁻² s⁻¹, which is the 24-hour average value given by a detailed 1984 inventory of the model domain [*Aerovironment, Inc.*, 1984]. This value is about half the NAPAP value, reflecting a real decrease in SO_2 emissions between 1980 and 1984 due to the installation of scrubbers (F. Hagist, Texaco Oil Company, personal communication, 1984). High NH_3 emissions are expected from agricultural and livestock activities around Bakersfield, but no local emission inventory is available. We assume a constant NH_3 emission rate of 2.5×10^{11} molecules cm⁻² s⁻¹, which was adjusted to fit the N(-III) concentrations observed at Bakersfield. This emission rate is reasonably consistent with the mean value of 4.1×10^{11} molecules cm⁻² s⁻¹ estimated by *Jacob* [1985] for the southern San Joaquin Valley on the basis of livestock populations, fertilizer use, and soil types. Vehicular emissions of formic and acetic acids are included in the model on the basis of measured RCOOH/CO emission ratios for automobile exhaust [*Talbot et al.*, 1988].

2.2. Aqueous-Phase Chemical Mechanism

Additions and modifications to the *Jacob* [1986] mechanism are listed in Table 3. The main changes are (1) addition of transition metal chemistry and (2) revision of sulfur chemistry to incorporate new kinetic data. Rate constants of ion-ion reactions are corrected for ionic strength with the Debye-Huckel equation, and equilibrium constants are corrected with the Davis equation [*Stumm and Morgan*, 1981]. The cloud water ionic strengths in the simulation are of the order of 0.01-0.1 M; therefore ionic strength corrections are necessary. The aqueous-phase redox reactions of NO, NO_2, and CO_3^- have been deleted from the original *Jacob* [1986] mechanism because they play a negligible role in the model chemistry. The aqueous-phase chemistry of NO_3 is also ignored in view of evidence that the solubility of NO_3 in water is low [*Mozurkewich*, 1986].

Redox reactions of dissolved trace metals can play important roles in the oxidation of S(IV) and in the odd hydrogen budget [*Graedel et al.*, 1986]. Our simulation of aqueous-phase transition metal chemistry draws heavily from the work of *Graedel et al.* [1986] and *Wechsler et al.* [1986] and includes a number of modifications and updates. We assume that Fe, Mn, and Cu are the only transition metals chemically active in the aqueous phase and that their reactivities are those of the redox couples Fe(II)/Fe(III), Mn(II)/Mn(III), and Cu(I)/Cu(II). From equilibrium considerations, we expect Fe(II), Mn(II), Cu(I), and Cu(II) in cloud water to be mainly present as free ions [*Hoffmann and Jacob*, 1984; *Wechsler et al.*, 1986], while Fe(III) and Mn(III) should be in complexed form. Iron(III) forms hydroxy and sulfate complexes and precipitates as $Fe(OH)_3$ at high pH; we assume that all soluble Fe(III) complexes have similar reactivities and that

Fe(OH)$_3$ is chemically inert. The fraction of precipitated Fe(III) is computed from the equilibria in Table 3. Manganese(III) should e mainly present as the hydroxy complex Mn(OH)$^{2+}$, whose reactivity differs substantially from that of Mn^{3+} [Davies, 1969]. When available, reaction rate constants specific to Mn(OH)$^{2+}$ are used in the mechanism.

Oxidation of S(IV) by Fe(III) and Mn(II) can be an important source of S(VI) at the concentration and pH ranges found in clouds [Jacob and Hoffmann, 1983]. By comparison, oxidation by Cu(II) is negligibly slow at pH < 7 [Conklin and Hoffmann, 1988b]. The mechanism of the S(IV) + Fe(III) reaction is still the subject of controversy. Conklin and Hoffmann [1988a] proposed a nonradical mechanism in which Fe(III) acts as a catalyst for the autoxidation of S(IV):

$$\text{(R1)} \qquad SO_3^{2-} + Fe(III) \xrightarrow{\quad H_2O, O_2 \quad} SO_4^{2-} + Fe(III) + H_2O_2$$
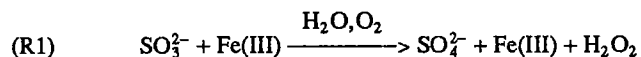
This mechanism produces H$_2$O$_2$ which then reacts with S(IV), effectively doubling the S(VI) yield. However, Martin [1988] found evidence for radical formation in the S(IV) + Fe(III) reaction. He proposed a radical mechanism in which S(IV) is directly oxidized by Fe(III),

$$\text{(R2)} \qquad SO_3^{2-} + Fe(III) \longrightarrow SO_3^- + Fe(II)$$
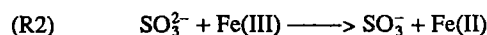
initiating the radical-assisted S(IV) oxidation chain propagated by reactions of SO$_3^-$, SO$_5^-$, SO$_4^-$, and Cl$_2^-$.

The choice of mechanism for the S(IV) + Fe(III) reaction has two important implications for computing S(VI) production rates. First, the sulfate yield differs depending on the mechanism. Second, the radical mechanism reduces Fe(III) while the nonradical mechanism does not. If the radical mechanism is correct, then Fe(II) must be reoxidized by a separate route in order to sustain the S(IV) + Fe(III) reaction. In the standard simulation we assume that both the S(IV) + Fe(III) and the S(IV) + Mn(II) reactions follow the nonradical mechanism. A sensitivity calculation will be conducted using the radical mechanism.

Gas-droplet transfer fluxes are computed for a monodisperse cloud with droplet radius of 10 μm, and mass accommodation coefficients $\gamma = 0.1$ for all soluble species. The assumption of $\gamma = 0.1$ yields accurate fluxes as long as the actual value of γ ranges between 0.05 and 1 [Jacob, 1986]. Recent measurements indicate that mass accomodation coefficients of highly soluble species fall within this range, namely, $\gamma_{SO2} = 0.11$ and $\gamma_{H2O2} = 0.18$ on clean water droplets [Worsnop et al., 1989], $\gamma_{HO2} > 0.2$ on aqueous (NH$_4$)$_2$SO$_4$ aerosol [Mozurkewich et al., 1987], and $\gamma_{OH} = 1$ on ice and H$_2$SO$_4$ surfaces [Gershenzon et al., 1986]. Accommodation coefficients for less soluble species such as O$_3$ may be much lower [Tang and Lee, 1987], but these species equilibrate rapidly between the gas and droplet phases so accurate computation of transfer fluxes is less important [Chameides, 1984; Schwartz, 1988].

2.3. Radiation Field

Calculation of photolysis rates requires solution to the equation of radiative transfer for an atmosphere containing a cloud layer. Most previous photochemical models have avoided this difficulty by assuming arbitrary correction factors which were applied to the clear-sky photolysis rate constants [Chameides and Davis, 1982; Graedel and Goldberg, 1983; Schwartz, 1984; Jacob, 1986; McElroy, 1986a; Graedel et al., 1986]. One exception is Chang et al. [1987], who computed the radiation field in the cloudy atmosphere using the delta-Eddington approximation [Joseph et al., 1976]. We present here a more comprehensive method of solving for the

radiation field in an inhomogeneous, Mie-scattering, plane-parallel atmosphere (simulating a stratus cloud). The technique is based on the multi-stream method of Feautrier [1964] which has been extended to the general case of anisotropic scattering by L. H. Auer and M. J. Prather (unpublished, see applications by Cochran and Trafton, [1978] and Logan et al., [1981]). In this section we summarize the physical and optical properties of the cloud entering into the calculation of photolysis rates, and present results specific to the simulation of the Bakersfield episode. Complete descriptions of the optical properties of the cloud derived from Mie theory, and of the method of solving the equation of radiative transfer, are presented in the appendix. Also shown in the appendix are detailed calculations which highlight the critical variables controlling photolysis rates in the presence of planar clouds.

For the purpose of calculating the UV and visible radiation field, the cloud is treated as a polydisperse gamma distribution of spheres of pure H$_2$O with an effective radius of 10 μm. Such a distribution is typical of water clouds and gives a Mie scattering function that is only weakly dependent on wavelength [see Deirmendjian, 1969]. (N.B., computation of gas-droplet mass transfer rates in the chemical model assumes for convenience a monodisperse cloud with droplet radius of 10 μm; cf. section 2.2.) The total liquid water column of the daytime stratus cloud in the simulation is 24 g m^{-2} (Figure 2), so that the vertically integrated geometric cross section per unit area for the assumed droplet size distribution is 1.8 (dimensionless: m^2 m^{-2}).

The optical properties of the cloud are derived from Mie scattering theory for spheres of pure H$_2$O, assuming that all light is unpolarized (A. Lacis, Goddard Institute of Space Studies, personal communication, 1988; cf. Hansen and Travis, [1974]). The Mie phase function has a strong forward peak associated with diffraction of light around the droplets that cannot be adequately resolved by decomposition of the phase function into orthogonal polynomials, and is therefore truncated (i.e., very small angle scattering is treated as a non-event). For this renormalized phase function, the ratio of optical to geometric cross section, Q, is about unity for wavelengths between 300 and 600 nm (instead of 2 for the true Mie phase function), and the total optical depth of the cloud (τ_{ex}^*) is about 2 instead of 4 (cf. appendix).

The solution for the radiation field in the cloudy atmosphere uses an 80-stream approximation to the Mie phase function. The atmosphere is assumed to consist of 900 mbar of clear, Rayleigh scattering atmosphere above the stratus cloud and 100 mbar below it; molecular scattering and absorption within the cloud are ignored. The total Rayleigh optical depth ranges from 1.0 at 310 nm to 0.3 at 400 nm, and the renormalized optical depth of the cloud, as noted above, is assumed to be 2.0. At 310 nm, stratospheric ozone has an absorption optical depth of about 1 that is included in the uppermost layers. A ground reflectivity (Lambertian) of 0.10 is assumed.

In the photochemical model the photolysis rates are calculated on-line with an algorithm which includes the effects of ozone absorption and molecular scattering [Prather, 1974; Logan et al., 1981], but not clouds. The computation is similar to that described in the appendix except that scattering is resolved by a six-stream Rayleigh phase function, rather than by the 80-stream Mie phase function. The simulation of cloud scattering is computationally more expensive by 2 orders of magnitude; we choose therefore to conduct these calculations off-line and use the results to define correction factors which are applied in the photochemical model to the clear-sky photolysis rates calculated for the Rayleigh atmosphere. The correction factors are the ratios of the monochromatic radiation intensities (J values) for the cloudy at-

TABLE 3a. Modifications and Additions to the *Jacob* [1986] Aqueous-Phase
Chemistry Mechanism: Henry's Law Constants

	K_{H298}, M atm^{-1}	ΔH_{298}, kcal mol^{-1}	Reference
CH$_3$C(O)CHO	3.7(3)^a	-15.0	*Betterton and Hoffmann* [1988a]
CH$_3$C(O)OOH	4.7(2)	-12.3	*Lind and Kok* [1986]
CH$_3$COOH	8.8(3)	-12.8	*Weast* [1986]
CHOCHO	3.(5)^b	0.*	*Betterton and Hoffmann* [1988a]
HNO$_4$	2.(4)	0.*	*Park and Lee* [1987]

Read 3.7(3) as 3.7x10^3. Reaction rates are first-order in each of
the species on the left-hand of the reaction equation, to the exclu-
sion of other species. Species above the reaction sign are reactants
which do not enter into the rate expression, generally because they
are involved in a non limiting step of the overall reaction.
Estimated values are flagged with an asterisk. Unknown activa-
tion energies are estimated as described by Jacob (1986).

  ^{a} Equilibrium with the hydrated form: CH$_3$COCHO(g) =
CH$_3$COCH(OH)$_2$

  ^{b} Lower limit for equilibrium with the hydrated forms GLYXA
(cf. Table 1).

mosphere to the corresponding J values for clear sky and are
determined locally as a function of the renormalized total cloud
optical depth (τ_{cx}^*), the overhead cloud optical depth for the partic-
ular layer ($\tau^*(z) < \tau_{cx}^*$) and the solar zenith angle ($\theta = \cos^{-1}\mu$).
The value of $\tau^*(z)$ is computed by adding the renormalized optical
depths $\Delta\tau^*$ of the individual cloudy layers overhead; $\Delta\tau^*$ is related
to the liquid water content of the layer, W (grams of liquid water
per cubic meter of air) and the layer thickness, ΔZ (meters), as fol-
lows (cf. appendix):

$$\Delta\tau^* = 0.08W\Delta Z \tag{1}$$

The correction factor at 310 nm is applied to the rate of the photo-
lysis reaction O$_3$ + $h\nu$ → O$_2$ + O^{1}D, and the correction factor at
400 nm is applied to all other photolysis rates. Figure 3 shows the
correction factors in the simulation at noon, as a function of alti-
tude.

Aqueous-phase photolysis rates are determined by the radiation
field within the cloud droplets, which can differ substantially from
that outside because of reflection and refraction at the air-droplet
interface and because of internal reflections within the droplet.
Madronich [1987] computed a radiative enhancement of 57%
within a pure water droplet relative to outside as a result of refrac-
tion and internal reflections. We did not include this radiative
enhancement in the model calculations; the effect on model results
is insignificant since aqueous-phase photolysis reactions play only
a minor role in the chemistry of interest.

2.4. Below-Cloud Aerosol

The below-cloud aerosol is simulated as a chemically inert mix-
ture of aqueous ammonium salts ((NH$_4$)$_2$SO$_4$, NH$_4$S(IV),
NH$_4$NO$_3$), trace metals (Fe, Mn, Cu), and NaCl. This aerosol is
explicitly included in the model in order to (1) simulate the tran-
sport of non-volatile species below cloud base, (2) supply the nu-
clei for cloud droplet formation, and (3) account for the partition-
ing of N(-III) and N(V) between the gas phase and the aerosol in

TABLE 3b. Modifications and Additions to the *Jacob* [1986]
Aqueous-Phase Chemistry Mechanism: Aqueous-Phase Equilibria

	K_{298}, M^n	ΔH_{298}, kcal mol^{-1}	Reference
CH$_3$COCHO + H$_2$O = CH$_3$COCH(OH)$_2$	2.7(3)	0.*	*Wasa and Musha* [1970]
CH$_3$COOH = CH$_3$COO$^-$ + H$^+$	1.7-(5)	-0.1	*Martell and Smith* [1977]
HNO$_4$ = NO$_4^-$ + H$^+$	1.0(2)	0.*	*Park and Lee* [1987]
Fe^{2+} + OH$^-$ = Fe(OH)$^+$	3.2(4)	0.*	*Turner et al.* [1981]
Fe^{3+} + SO$_4^{2-}$ = FeSO$_4^+$	1.4(4)	6.2	*Sillen and Martell* [1964]
Fe^{3+} + SO$_3^{2-}$ = FeSO$_3^+$	4.0(6)	0.*	*Conklin and Hoffmann* [1988a]
Fe(OH)$^{2+}$ + SO$_3^{2-}$ = FeHOSO$_3$	2.0(7)	0.*	*Conklin and Hoffmann* [1988a]
Fe^{3+} + OH$^-$ = Fe(OH)$^{2+}$	6.3(11)	-6.3	*Flynn* [1984]
Fe^{3+} + 2OH$^-$ = Fe(OH)$_2^+$	2.0(22)	-4.6	*Flynn* [1984]
Fe^{3+} + 3OH$^-$ = Fe(OH)$_3$	1.3(37)	-20.7	*Flynn* [1984]; *Latimer* [1952]
Mn^{3+} + OH$^-$ = Mn(OH)$^{2+}$	2.5(14)	-8.5	*Smith and Martell* [1976]

Read 2.7(3) as 2.7x10^3. Reaction rates are first-order in each of the species on the left-hand of
the reaction equation, to the exclusion of other species. Species above the reaction sign are reac-
tants which do not enter into the rate expression, generally because they are involved in a non limit-
ing step of the overall reaction. Estimated values are flagged with an asterisk. Unknown activation
energies are estimated as described by Jacob (1986).

TABLE 3c. Modifications and Additions to the *Jacob* [1986]
Aqueous-Phase Chemistry Mechanism: Aqueous-Phase Reaction Rate Constants

	k_{298}, M^n s^{-1}	E_a kcal mol^{-1}	Reference
Hydrocarbons			
$CH_3COOH + OH \xrightarrow{O_2} HO_2 + CO + CH_2O + H_2O$	2.(7)	3.7*	*Fharataziz and Ross* [1977]
$CH_3COO^- + OH \xrightarrow{O_2} O_2^- + CO + CH_2O + H_2O$	8.(7)	3.*	*Fharataziz and Ross* [1977]
$GLYXA + OH \xrightarrow{O_2} HO_2 + 2CO + nH_2O$	4.(8)	3.*	*Fharataziz and Ross* [1977]
$MGLYA + OH \xrightarrow{O_2} CH_3CO_3 + CO + nH_2O$	4.(8)*	3.*	*a*
Odd Nitrogen			
$HNO_4 \rightarrow HNO_2 + O_2$	1.(-2)	0.*	*Park and Lee* [1987]
$NO_4^- \rightarrow NO_2^- + O_2$	1.(-2)	0.*	*Park and Lee* [1987]
Sulfur			
$GLYXA + HSO_3^- \rightarrow GMBS$	1.3(-1)	14.9*	*Olson and Hoffmann* [1988]
$GLYXA + SO_3^{2-} \xrightarrow{H_2O} GMBS + OH^-$	2.1(3)	9.2*	*Olson and Hoffmann* [1988]
$GMBS + SO_3^{2-} \rightarrow GDBS$	2.0(4)	7.8*	*b*
$GDBS \rightarrow GMBS + HSO_3^-$	1.1(-5)	0.*	*Olson and Hoffmann* [1988]
$GDBS + OH^- \rightarrow GMBS + SO_3^{2-} + H_2O$	8.8(6)	4.2*	*Olson and Hoffmann* [1988]
$GMBS \rightarrow GLYXA + HSO_3^-$	4.6(-6)	0.*	*Olson and Hoffmann* [1988]
$GMBS + OH^- \rightarrow GLYXA + SO_3^{2-} + H_2O$	9.7(5)	5.5*	*Olson and Hoffmann* [1988]
$MGLYA + HSO_3^- \rightarrow HAMS$	1.3(0)	6.9	*Betterton and Hoffmann* [1987]
$MGLYA + SO_3^{2-} \xrightarrow{H_2O} HAMS + OH^-$	1.4(5)	4.4	*Betterton and Hoffmann* [1987]
$HAMS + OH^- \rightarrow MGLYA + SO_3^{2-} + H_2O$	1.3(7)	-1.2	*c*
$HAMS \rightarrow MGLYA + HSO_3^-$	4.2(-6)	19.6	*Betterton and Hoffmann* [1987]
$SO_3^{2-} + O_2^- \xrightarrow{2H_2O} SO_3^- + H_2O_2 + 2OH^-$	8.2(1)	11.*	*Sadat-Shafai et al.* [1981]
$HSO_3^- + OH \rightarrow SO_3^- + H_2O$	4.5(9)	3.*	*Huie and Neta* [1987]
$SO_3^{2-} + OH \rightarrow SO_3^- + OH^-$	5.2(9)	3.*	*Huie and Neta* [1987]
$HMS + OH \rightarrow CH_2O + SO_3^- + H_2O$	1.3(9)	3.*	*Martin et al.* [1989]
$GMBS + OH \rightarrow SO_3^- + GLYXA + H_2O$	1.3(9)*	3.*	*d*
$GDBS + OH \rightarrow SO_3^- + HSO_3^- + GLYXA + H_2O$	1.3(9)*	3.*	*d*
$HAMS + OH \rightarrow SO_3^- + MGLYA + H_2O$	1.3(9)*	3.*	*d*
$HSO_3^- + Cl_2^- \rightarrow SO_3^- + 2Cl^- + H^+$	3.4(8)	3.*	*Huie and Neta* [1987]
$SO_3^{2-} + Cl_2^- \rightarrow SO_3^- + 2Cl^-$	3.4(8)	3.*	*Huie and Neta* [1987]
$CH_3C(O)OOH + HSO_3^- + H^+ \rightarrow CH_3COOH + SO_4^{2-} + 2H^+$	3.6(7)	7.9	*Lind et al.* [1987]
$CH_3C(O)OOH + HSO_3^- \rightarrow CH_3COOH + SO_4^{2-} + H^+$	7.0(2)	7.9	*Lind et al.* [1987]
$HSO_5^- + HSO_3^- + H^+ \rightarrow 2SO_4^{2-} + 3H^+$	7.1(6)	6.2	*Betterton and Hoffmann* [1988b][e]
$SO_5^- + HSO_3^- \rightarrow SO_4^- + SO_4^{2-} + H^+$	7.5(4)	7.0*	*Huie and Neta* [1987]
$SO_5^- + HSO_3^- \rightarrow HSO_5^- + SO_3^-$	2.5(4)	7.7*	*Huie and Neta* [1987]
$SO_5^- + SO_5^- \rightarrow 2SO_4^- + O_2$	6.0(8)	3.*	*Huie and Neta* [1987]
$Fe(III)_{aq} + SO_3^{2-} \xrightarrow{H_2O, O_2} Fe(III) + SO_4^{2-} + H_2O_2$	9.5(7)	12.*	*f*
$Mn(II) + HSO_3^- \xrightarrow{H_2O, O_2} Mn(II) + SO_4^{2-} + H_2O_2 + H^+$	1.0(3)	17.8	*g*
$SO_4^- + Fe(II) \rightarrow SO_4^{2-} + Fe(III)$	9.9(8)	3.*	*Heckel et al.* [1966]
$SO_4^- + Mn(II) \rightarrow SO_4^{2-} + Mn(III)$	1.8(10)	3.*	*Lee and Rochelle* [1987]
$SO_4^- + Cu(I) \rightarrow SO_4^{2-} + Cu(II)$	9.9(8)	3.*	*h*
$SO_4^- \xrightarrow{H_2O} SO_4^{2-} + H^+ + OH$	3.6(2)	0.*	*Tang et al.* [1989]
$SO_4^- + HSO_3^- \rightarrow SO_4^{2-} + H^+ + SO_3^-$	7.5(8)	3.*	*Wine et al.* [1989]
$SO_4^- + NO_2^- \rightarrow SO_4^{2-} + NO_2$	9.8(8)	3.*	*Wine et al.* [1988a]
$SO_4^- + CH_3OH \xrightarrow{O_2} SO_4^{2-} + H^+ + CH_2O + HO_2$	8.8(6)	4.2*	*Wine et al.* [1989]
$SO_4^- + HCOO^- \xrightarrow{O_2} SO_4^{2-} + CO_2 + HO_2$	1.1(8)	3.*	*Wine et al.* [1989]
$SO_4^- + HCOOH \xrightarrow{O_2} SO_4^{2-} + CO_2 + HO_2 + H^+$	4.6(5)	6.0*	*Wine et al.* [1989]

TABLE 3. (continued)

Reaction	k_{298}, M^n s^{-1}	E_a kcal mol^{-1}	Reference
$SO_4^- + CH_3COO^- \xrightarrow{O_2} SO_4^{2-} + CO_2 + CH_3O_2$	3.7(6)	4.7*	Wine et al. [1989]
$SO_4^- + CH_3COOH \xrightarrow{O_2} SO_4^{2-} + CO_2 + CH_3O_2 + H^+$	1.4(4)	8.0*	Wine et al. [1989]
$SO_4^- + Cl^- \rightarrow SO_4^{2-} + Cl$	2.6(8)	3.*	Wine et al. [1989]
$Cl \xrightarrow{H_2O} Cl^- + H^+ + OH$	1.(5)	0.*	Wine et al. [1989]
Fe(II)/Fe(III)			
$Fe(II) + OH \rightarrow Fe(III) + OH^-$	3.(8)	3.*	Fharataziz and Ross [1977]
$Fe(II) + HO_2 \xrightarrow{H_2O} Fe(III) + H_2O_2 + OH^-$	1.2(6)	5.4*	Rush and Bielski [1985]
$Fe(II) + O_2^- \xrightarrow{2H_2O} Fe(III) + H_2O_2 + 2OH^-$	1.0(7)	4.1*	Rush and Bielski [1985]
$Fe(OH)^+ + H_2O_2 \rightarrow Fe^{3+} + OH + 2OH^-$	1.9(6)	12.4	Moffett and Zika [1987]
$Fe(II) + O_3 \xrightarrow{H_2O} Fe(III) + OH + OH^- + O_2$	1.7(5)	6.5*	Conocchioli et al. [1965]
$Fe(II) + Cl_2^- \rightarrow Fe(III) + 2Cl^-$	1.0(7)	5.4	Thornton and Laurence [1973][i]
$\rightarrow Fe(III) + 2Cl^-$	4.0(6)	7.5	Thornton and Lawrence [1973][i]
$Fe(III)_{aq} + HO_2 \rightarrow Fe(II) + H^+ + O_2$	2.0(4)	7.8*	Bielski et al. [1985]
$Fe(III)_{aq} + O_2^- \rightarrow Fe(II) + O_2$	1.5(8)	3.*	Rush and Bielski [1985]
$Fe^{3+} + hv \xrightarrow{H_2O} Fe^{2+} + OH + H^+$	9.6(-7)		Wechsler et al. [1986][j]
$Fe(OH)^{2+} + hv \rightarrow Fe^{2+} + OH$	5.9(-4)		Wechsler et al. [1986][j]
$Fe(OH)_2^+ + hv \rightarrow Fe^{2+} + OH + OH^-$	5.8(-4)		Wechsler et al. [1986][j]
Mn(II)/Mn(III)			
$Mn(II) + OH \rightarrow Mn(III) + OH^-$	3.4(7)	3.4*	Pick-Kaplan and Rabani [1976]
$Mn(II) + HO_2 \xrightarrow{H_2O} Mn(III) + H_2O_2 + OH^-$	6.(6)	4.4*	Cabelli and Bielski [1984]
$Mn(II) + O_2^- \xrightarrow{2H_2O} Mn(III) + H_2O_2 + 2OH^-$	1.1(8)	3.*	Pick-Kaplan and Rabani [1976)]
$Mn(II) + Cl_2^- \rightarrow Mn(III) + 2Cl^-$	1.4(7)	8.1	Laurence and Thornton [1973]
$Mn(III) + HO_2 \rightarrow Mn(II) + O_2 + H^+$	2.0(4)*	7.8*	k
$Mn(III) + O_2^- \rightarrow Mn(II) + O_2$	1.5(8)*	3.*	k
$Mn(III) + H_2O_2 \rightarrow Mn(II) + HO_2 + H^+$	3.2(4)	7.5*	Davies [1969]
$Mn(III) + Fe(II) \rightarrow Mn(II) + Fe(III)$	2.1(4)	7.8*	Davies [1969]
$Mn(III) + Cu(I) \rightarrow Mn(II) + Cu(II)$	2.1(4)*	7.8*	l
Cu(I)/Cu(II)			
$Cu(I) + OH \rightarrow Cu(II) + OH^-$	3.(8)*	3.*	m
$Cu(I) + HO_2 \xrightarrow{H_2O} Cu(II) + H_2O_2 + OH^-$	1.5(9)	3.*	Bielski et al. [1985]
$Cu(I) + O_2^- \xrightarrow{2H_2O} Cu(II) + H_2O_2 + 2OH^-$	1.(10)	3.*	Rabani et al. [1973]
$Cu(I) + H_2O_2 \rightarrow Cu(II) + OH + OH^-$	4.(5)	6.2	Moffett and Zika [1987]
$Cu(I) + Cl_2^- \rightarrow Cu(II) + 2Cl^-$	1.4(7)*	6.4*	n
$Cu(II) + HO_2 \rightarrow Cu(I) + O_2 + H^+$	1.(8)	3.*	Rabani et al. [1973]
$Cu(II) + O_2^- \rightarrow Cu^+ + O_2$	5.(9)	3.*	Bielski et al. [1985]

Read 2.(7) as 2.0×10^7. Reaction rates are first-order in each of the species on the left-hand of the reaction equation, to the exclusion of other species. Species above the reaction sign are reactants which do not enter into the rate expression, generally because they are involved in a non limiting step of the overall reaction. Estimated values are flagged with an asterisk. Unknown activation energies are estimated as described by *Jacob* [1986].

[a] The value for GLYXA+OH is assumed.

[b] Derived from *Olson and Hoffmann* [1988a] data for GMBS + HSO_3^- = GBDS (K=1.45×10^4 M) and GDBS + $OH^- \rightarrow$ GMBS + HSO_3^- (k=8.8×10^6 M^{-1} s^{-1}). We assume that the equilibrium GMBS + HSO_3^- = GDBS represents a balance between forward reaction GMBS + SO_3^{2-} and back reaction GDBS + OH^-. The rate constant for GMBS + SO_3^{2-} is then given by kKK_w/K_{a2}, where K_w and K_{a2} are the acid dissociation constants for H_2O and HSO_3^-, respectively.

[c] Derived from *Betterton and Hoffmann* [1987] data for $CH_3COCH(O^-)SO_3^- \rightarrow CH_3COCHO + SO_3^{2-}$ (k_{298}=$6.8 \times 10^3 s^{-1}$, E_a= 16.9 kcal $mole^{-1}$) and $CH_3COCH(OH)SO_3^-$ = $CH_3COCH(O^-) SO_3^- + H^+$($K_a$=$1.9 \times 10^{-11}$ M, ΔH=-4.8 kcal $mole^{-1}$), and the H_2O acid dissociation constant. The negative value for the apparent E_a results from the enthalpies of the participating equilibria.
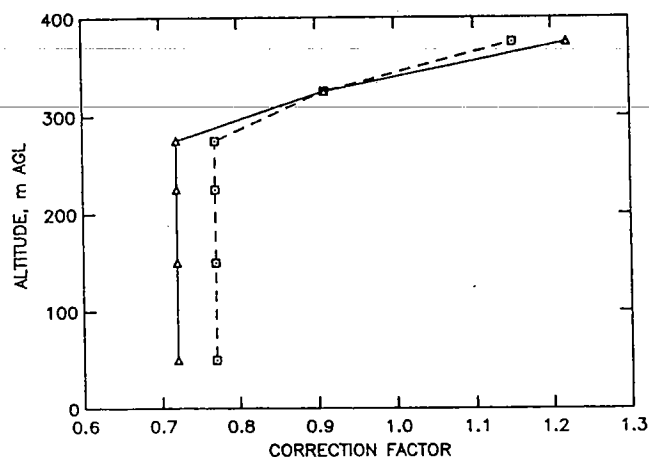
Fig. 3. Correction of radiation intensities at 400 nm (solid line) and at 310 nm (dashed line) for the presence of cloud, as a function of altitude. The correction factors represent the ratios of the radiation intensities in the cloudy atmosphere to the clear-sky values.

layer 1 (which affects their deposition velocities). Aerosol particles are assumed to be 100% scavenged by cloud droplets upon cloud formation; i.e., no interstitial aerosol is allowed in cloud [ten Brink et al., 1987].

Ammonium-S(IV) aerosol is formed in the model by evaporation of cloud droplets containing HMS, HAMS, GMBS, and GDBS. The assumption that S(IV)-carbonyl ammonium salts are non volatile is reasonable at least for HMS since hydroxymethanesulfonic acid is a strong acid [Roberts et al., 1971], and the dissociated form is therefore likely to remain in aqueous aerosol following cloud evaporation. Aqueous NH_4NO_3 aerosol is formed by condensation of HNO_3 with the NH_3 remaining in excess after titration of S(VI) and S(IV)-carbonyl adducts. The partial pressures of NH_3 and HNO_3 over the aqueous NH_4NO_3 aerosol are computed as described by Russell et al. (1983).

Aerosol concentrations of Fe, Mn, and Cu are held fixed throughout the simulation at the mean values measured in Bakersfield fog water during January 1984, scaled by the liquid water content (Table 2). Following Wechsler et al. [1986], we assume that 30% of cloud water/ Fe, Mn, and Cu is readily soluble. In Bakersfield fog samples, most of these metals were found to pass through a 0.2-μm pore filter (D. J. Jacob, unpublished results, 1985), suggesting that significant fractions are indeed soluble.

The two oxidation states of each metal are transported as separate species, and the partitioning between the two states is allowed to evolve over the course of the simulation as a result of aqueous-phase reactions in the cloud.

Concentrations of Cl⁻ are held fixed at the mean values observed in Bakersfield aerosol during the January 1984 field experiment (Table 2). A matching concentration of a chemically inert cation, e.g., Na^+, is assumed. The species Cl⁻, Cl, and Cl_2^- are not transported separately in the model because (1) they are in rapid equilibrium with each other and (2) the contributions of Cl and Cl_2^- to total chlorine are small.

2.5. Computational Procedure

The results presented below are from 72-hour simulations beginning on January 3, 1984 at 0000 local time, which is defined as the onset of the stagnation episode. Initial concentrations (Table 2) are specified on the basis of observations when available, and from typical regional background concentrations otherwise. The model computes the chemical evolution of atmospheric composition in layer k by solving the general diffusion equations discretized in space for m_k independent gas-phase and aqueous-phase species. The value of m_k depends on whether layer k is cloudy or clear since aqueous-phase species are present only in cloud. The set of independent species includes all gas-phase species of the detailed Lurmann et al. [1986] mechanism, plus the class I and class II aqueous-phase species of Table 4. Aqueous-phase species in classes III-IV-V of Table 4 are treated as dependent variables, with concentrations constrained by equilibrium with the gas phase (class III), steady state (class IV), or the electroneutrality equation (class V). Use of computational constraints for aqueous-phase species in classes III-IV-V saves computer time at negligible loss in accuracy.

The change with time in the concentration $n_{i,k}(t)$ (molecules per cubic centimeter) of independent species i in layer k is given by

$$k = 2,3,4,5$$

$$\frac{dn_{i,k}(t)}{dt} = P_{i,k}[n_{j,k}(t)] - L_{i,k}[n_{j,k}(t)]$$

$$- \frac{2K_k <N_k>}{z_{k+1}-z_{k-1}} \left(\frac{n_{i,k}(t)/N_k - n^*_{i,k+1}(t)/N_{k+1}}{z_{k+1}-z_k} \right)$$

$$- \frac{2K_{k-1} <N_{k-1}>}{z_{k+1}-z_{k-1}} \left(\frac{n_{i,k}(t)/N_k - n^*_{i,k-1}(t)/N_{k-1}}{z_k-z_{k-1}} \right) \qquad (2a)$$

[d] The value for HMS+OH is assumed [Martin et al., 1989].

[e] McElroy [1987] reports as preliminary values for this reaction $k_{298}=2.7\times10^7$ $M^{-2}s^{-1}$ and $E_a = 1.2$ kcal mol^{-1}.

[f] Stoichiometry from Conklin and Hoffmann [1988a], rate constant at zero ionic strength from Martin and Hill [1987a].

[g] Rate constant at zero ionic strength from Martin and Hill [1987b], activation energy from Hoffmann and Calvert [1985].

[h] Value for SO_4^- + Fe(II) is assumed.

[i] Reaction proceeds by competing outer-sphere and inner-sphere pathways, with different activation energies.

[j] Photolysis rates for 375m AGL (top of cloud) at noon. These values are the highest attained in the simulation.

[k] Values for $Fe(III)_{aq}$ + $O_2(-I)$ are assumed.

[l] Value for $Mn(OH)^{2+}$ + Fe^{2+} is assumed.

[m] Value for Fe^{2+} + OH is assumed.

[n] Value for Fe^{2+} + Cl^{2-} is assumed.

TABLE 4. Partitioning of Aqueous-Phase Species Into Computational Classes

Class	Species
Class I: independent species evaporating to the gas phase	$O_2(-I)$, OH, H_2O_2, $(HCOOH + HCOO^-)$, $(SO_2(aq) + HSO_3^- + SO_3^{2-})$, GLYXA, CH_3OOH
Class II: independent species evaporating to aerosol	S(VI), N(V), N(-III), Fe(II), Fe(III), Mn(II), Mn(III), Cu(I), Cu(II), HMS, HAMS, GMBS, GDBS, HSO_5^-, Cl^-, Na^+
Class III: species at equilibrium with gas phase	$(CH_2O + H_2C(OH)_2)$, MGLYA, $(HNO_2 + NO_2^-)$ $(H_2CO_3 + HCO_3^-)$, CH_3OH, $(CH_3COOH + CH_3COO^-)$, $CH_3C(O)COOH$
Class IV: species at steady state	SO_5^-, SO_4^-, O_3, $(Cl + Cl_2^-)$, $(HNO_4 + NO_4^-)$
Class V: species constrained by electroneutrality equation	H^+, OH^-

$k = 1$

$$\frac{dn_{i,1}(t)}{dt} = P_{i,1}[n_{j,1}(t)] - L_{i,1}[n_{j,1}(t)]$$

$$- \frac{2K_1 \langle N_1 \rangle}{z_1 + z_2} \left(\frac{n_{i,1}(t)/N_1 - n_{i,2}^*(t)/N_2}{z_2 - z_1} \right)$$

$$- \frac{2V_{d,i}}{z_1 + z_2} n_{i,1}(t) \tag{2b}$$

$k = 6$

$$\frac{dn_{i,6}(t)}{dt} = P_{i,6}[n_{j,6}(t)] - L_{i,6}[n_{j,6}(t)]$$

$$- \frac{K_5 \langle N_5 \rangle}{z_T - \frac{z_5 + z_6}{2}} \left(\frac{n_{i,6}(t)/N_6 - n_{i,5}^*(t)/N_5}{z_6 - z_5} \right)$$

$$- \frac{V_e}{z_T - \frac{z_5 + z_6}{2}} (n_{i,6}(t) - n_{i,T}) \tag{2c}$$

Here $P_{i,k}$ and $L_{i,k}$ are the chemical production and loss terms, respectively, which depend on the concentrations of the independent species $j = 1,...m_k$ in layer k; z_k is the layer midpoint; N_k is the air concentration (molecules per cubic centimeter) at altitude z_k; $\langle N_k \rangle$ is the air concentration at the boundary between layers k and $k+1$; K_k is the eddy diffusion coefficient between layer k and layer $k+1$; z_T is the upper boundary of the model domain; $V_{d,i}$ is the deposition velocity; V_e is the entrainment velocity at z_T; and $n_{i,T}$ is the concentration at z_T. The concentrations $n_{i,k-1}^*(t)$ and $n_{i,k+1}^*(t)$ in the eddy flux terms are identical to the actual concentrations $n_{i,k-1}(t)$ and $n_{i,k+1}(t)$ except in two cases: (1) Layer k is cloudy, layer $k-1$ is noncloudy, and i is a class I aqueous-phase species:

$$n_{i,k-1}^*(t) = 0 \tag{3a}$$

(2) Layer k is noncloudy, layer $k+1$ is cloudy, and i is a gas-phase species produced by evaporation of class I aqueous-phase species i':

$$n_{i,k+1}^*(t) = n_{i,k+1}(t) + n_{i',k+1}(t) \tag{3b}$$

The system of coupled equations (2) for all species and layers is integrated using an implicit finite difference method [Richtmeyer, 1957], with time steps of 15 min in the daytime and 1 hour at night. Radiation intensities are recalculated at 30-min intervals. We established in test simulations that these time steps are sufficiently small to ensure stable and accurate solutions.

3. OVERVIEW OF RESULTS

3.1. Sulfate, Nitrate, Ozone, Organic Acids

We compare in Figure 4 the simulated and observed time evolutions of sulfate, nitrate, and ammonium aerosol concentrations. Model results agree well with observations, although in the case of NH_4^+ this agreement is forced by the adjustment of the NH_3 source. The sulfate aerosol measurements of JMWH could have suffered from positive bias due to oxidation of S(IV) aerosol on the filter or during the filter extraction procedure. To account for this possibility we show in Figure 4 the simulated concentrations of both S(VI) and S(VI) + S(IV). The S(IV) concentrations in the model are small compared to S(VI) concentrations; hence there is little difference between the two plots.

Sulfate accumulates progressively over the course of the episode, due to the combination of restricted ventilation and sustained production by SO_2 oxidation. The concentration of SO_2 increases rapidly at the beginning of the episode and reaches after 1 day a steady state level of 18 ppb (Figure 5) which reflects mainly a balance between emissions and deposition. Model results for SO_2 are reasonably consistent with the daily average SO_2 concentrations of 10-28 ppb measured on January 4-5 at Texaco monitoring stations in Oildale just north of Bakersfield [F. Hagist, Texaco Oil Company, personal communication, 1984]. The mean boundary layer SO_2 oxidation rate in the model is about 1% h^{-1} at noon and 2 % h^{-1} at midnight; by comparison, JMWH estimated a range of 0.4-1.1% h^{-1} on the basis of observed S(VI) accumulation rates. Most of the S(VI) production in the model takes place in the
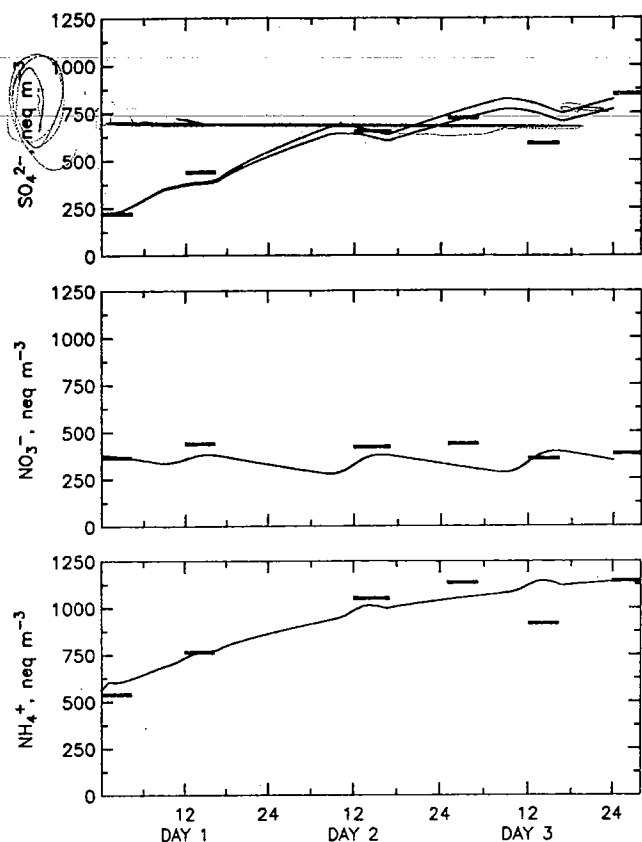
Fig. 4. Time evolution of sulfate, nitrate, and ammonium aerosol concentrations during the January, 3-5, 1984, episode (model days 1-3). Model results for layer 1 (solid lines) are compared to measurements at Bakersfield approximately 10 m above ground (data bars). In the case of sulfate, model results for both (S(VI)) and (S(VI))+2(S(IV)) are shown because of the possibility that sulfate aerosol measurements may be biased by oxidation of S(IV) on the filter sample.

stratus cloud (Figure 6). The mechanisms for S(VI) production will be discussed in detail in section 4.

By contrast to sulfate, nitrate does not accumulate over the course of the stagnation episode, even though NO_x concentrations rise to high levels both in the model (Figure 5) and in observations at Kernridge (JMWH). It appears that stagnant conditions do not provide a particularly favorable environment for the oxidation of NO_x to N(V), for two reasons. First, odd hydrogen is depleted at high NO_x concentrations, so that the rate of N(V) production by the reaction $NO_2 + OH$ increases only slowly with increasing NO_x concentration. Second, O_3 is titrated at night by large excesses of freshly emitted NO, preventing formation of NO_3 which is normally an important N(V) precursor in polluted atmospheres [Russell et al., 1986]. The only significant source of N(V) in the model is the reaction $NO_2 + OH$; this reaction is fastest in the stratus cloud because the radiation intensities, and hence the OH concentrations, are maximum (Figure 6).

The depletion of O_3 is a remarkable feature of the stagnation episode. Concentrations of O_3 in the simulation peak at only 4-5 ppb in the daytime and fall to essentially zero at night (Figure 5); observations at Kernridge on January 3-5 show a similar pattern, with daytime maxima of 3-10 ppb and nighttime concentrations below the detection limit of 2 ppb (JMWH). The photochemical production of O_3 within the boundary layer is inhibited by the accumulation of NO_x to high levels, while downward transport of O_3

from the free troposphere is restricted by the inversion. The low daytime O_3 concentrations reflect this suppression of the O_3 source combined with rapid removal of O_3 by deposition. In a test simulation with NO_x emissions reduced by half we found that the predicted daytime maxima of O_3 nearly tripled, demonstrating the strong quenching effect of excessive NO_x on O_3 production. At night, O_3 is depleted by reaction with NO, and the subsequent deposition of NO_2 removes odd oxygen from the boundary layer.

The simulated concentrations of HCOOH and CH_3COOH on model day 3 are 0.07 ppb and 0.04 ppb, respectively. By comparison, Munger et al. [1989] reported mean concentrations of 0.3 ppb for both acids at Bakersfield on the basis of simultaneous measurements of fog water concentrations, liquid water contents, and pH. Evidently, the model sources of organic acids are insufficient to account for these observations. In the model the major source of HCOOH is the aqueous-phase reaction $H_2C(OH)_2 + OH$, and the only significant source of CH_3COOH is emission from automobile exhaust. Ozonation of olefins is not a significant source of either acid because (1) O_3 concentrations are low, and (2) NO levels are sufficiently high that Criegee intermediates in the model react with NO instead of with H_2O [Atkinson and Lloyd, 1984]. The missing source(s) of organic acids could be of agricultural origin, e.g., emissions from cattle waste [Jain et al., 1986] or atmospheric oxidation of insecticide fumigants [Tuazon et al., 1984]. Bacterial oxidation of aldehydes in cloud droplets is another possible source. The inability of the model to simulate organic acid concentrations should not compromise other model results because organic acids are negligible contributors to the total acid budget even at the concentrations reported by Munger et al. [1989].
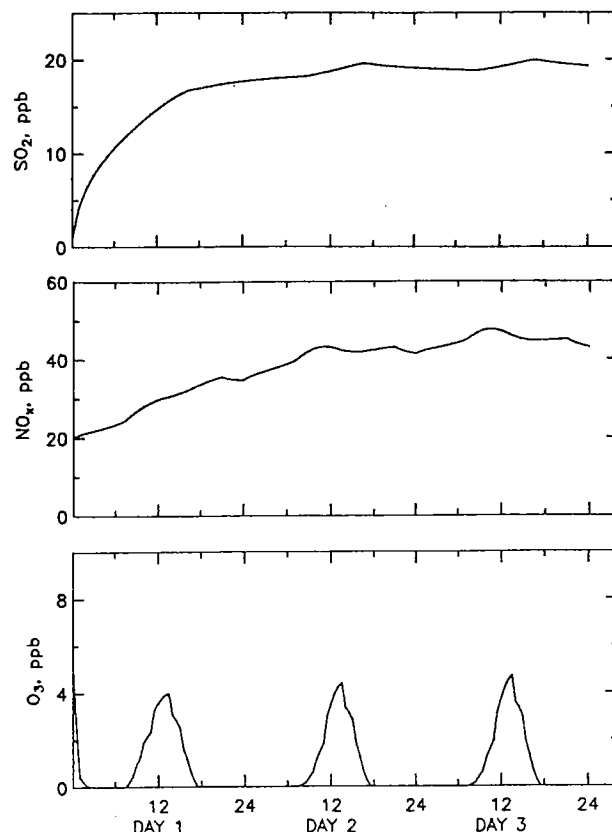

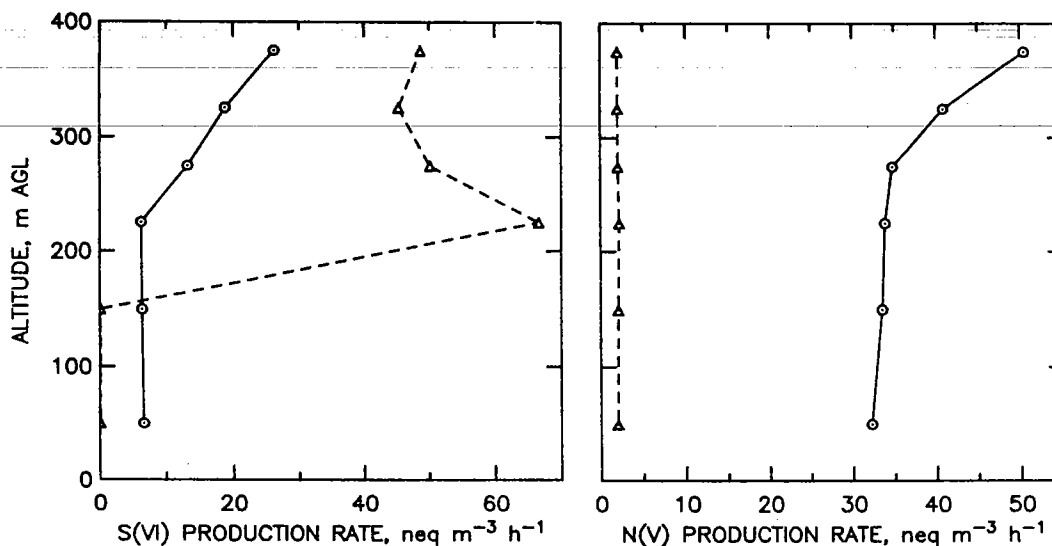Fig. 5. Time evolution of simulated SO_2, NO_x, and O_3 concentrations in layer 1.

Fig. 6. Vertical profiles of S(VI) and N(V) production rates on model day 3 at noon (solid line) and at midnight (dashed line).

3.2. Acid-Base Balance and Alkalinity

The rapid production of S(VI) in the model adds large amounts of acidity to the boundary layer atmosphere, but we find that this acidity is almost entirely neutralized by NH_3. Observations in Bakersfield indicate that NO_3^- and SO_4^{2-} in aerosol and fog water are generally 90-100% neutralized [*Munger et al.*, 1983; *Jacob et al.*, 1984; JMWH], in accord with model predictions. A striking feature of the Bakersfield observations, which is well simulated by the model, is that the total (aerosol + gas-phase) concentrations of acids and bases are usually in close balance. The equivalent ratio $\{(S(VI)) + (N(V))\}/(N(-III))$, which provides an approximate measure of this balance, remains near unity throughout the stagnation episode both in the model and in the observations (Figure 7). It appears therefore that N(-III) is present in amounts just sufficient to neutralize the acidity; there is little $NH_3(g)$ or $HNO_3(g)$ present in excess of the neutral aerosol. We will propose in section 5 an explanation for this close balance between acids and bases.

A quantitative measure of the acid-neutralizing capacity of the atmosphere is the atmospheric alkalinity, (ALK), which represents the deficiency of H^+ with respect to a reference "neutral" atmosphere. The concept of atmospheric alkalinity [*Liljestrand*, 1985; JMWH] is analogous to the concept of alkalinity commonly used in water chemistry [*Stumm and Morgan*, 1981]. We define here (ALK) by reference to the set of species (NH_4^+, NO_3^-, SO_4^{2-}, $S(IV)^-$, CO_2, RCOOH, H_2O). The value of (ALK) is computed by summing the concentrations of proton acceptors with respect to the reference species, and subtracting the concentrations of proton donors:

$$(ALK) = (NH_3(g)) + (HCOO^-) + (CH_3COO^-) + (HCO_3^-)$$

$$- (HNO_3(g)) - (HSO_4^-) - (H_2SO_4) - (H^+) \qquad (4)$$

where all concentrations are in equivalent units. The contributions to (ALK) from $HCOO^-$, CH_3COO^-, and HCO_3^- are small compared to the contribution from $NH_3(g)$; therefore (ALK) can be expressed to a good approximation by

$$(ALK) = (N(-III)) - (N(V)) - (S(IV)) - (S(VI)) \qquad (5)$$

We show in Figure 8 the simulated vertical distributions of (ALK) at noon and midnight on model day 3, computed from

equation (4). A remarkable result is that (ALK) changes sign within the boundary layer. The atmosphere near the ground contains net alkalinity, but the alkalinity decreases with altitude, and net inorganic acidity (negative alkalinity) is predicted for the upper portion of the boundary layer. The vertical trend of (ALK) reflects the opposite spatial distributions of NH_3 and acid sources: NH_3 is emitted at ground level, but S(VI) and N(V) are mostly produced within the cloud. From this result we draw the general conclusion that ground-based measurements of atmospheric acidity suffer from systematic bias because of the proximity of NH_3 sources. The air aloft may be acidic even though no net acidity is measured at the ground.

The small nonneutralized fraction of acidity in the simulated cloud is responsible for relatively low cloud water pH values, ranging from 4.2 at night to 3.4 in the early afternoon (Figure 9). The lower pH values in daytime are due mostly to gas-phase HNO_3 production by the reaction NO_2 + OH. The pH values predicted by the model can be compared to observations at McKittrick (Figure 1), where the cloud was sampled on January 3-5, 1984, as it intercepted the western slope of the valley. The measured cloud water pH values at McKittrick ranged from 2.7 to 5.2,
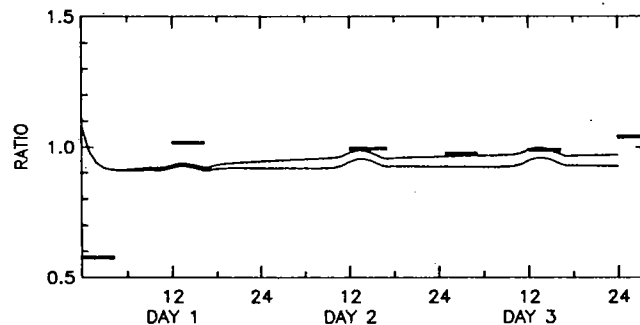

Fig. 7. Time evolution of the equivalent ratio $\{(S(VI))+(N(V))\}/(N(-III))$ during the January 3-5, 1984, episode (model days 1-3). Model results for layer 1 (solid lines) are compared to measurements at Bakersfield approximately 10 m above ground (data bars). The lower line accounts for the possibility that sulfate aerosol measurements may be biased by oxidation of S(IV) on the filter sample.
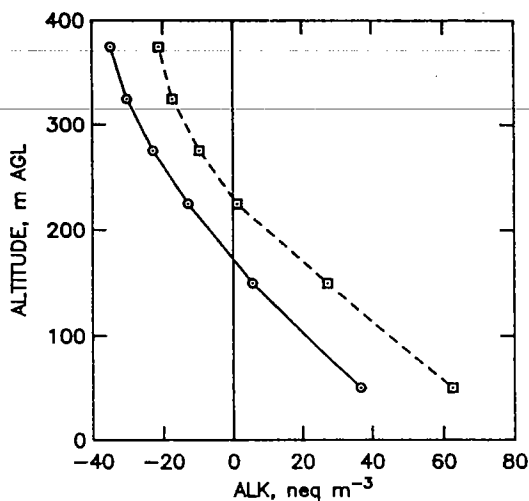
Fig. 8. Vertical profile of atmospheric alkalinity on model day 3 at noon (solid line) and at midnight (dashed line).

with a mean value of 4.0 [Jacob, 1985]. Model results are reasonably consistent with these observations, although the measured values are more variable and do not show a clear diurnal trend.

3.3. Odd Hydrogen Chemistry

We show in Figure 10 the vertical distributions of gas-phase OH, HO_2, and HNO_4 concentrations at noon on model day 3. The OH concentrations are comparable to the clean air value computed by Logan et al. [1981] for that latitude and season, but the HO_2 concentrations are 2 orders of magnitude lower because of the high NO levels. The most abundant odd hydrogen species is HNO_4, whose formation is favored by the combination of high NO_x levels and low temperatures. In cloud, HNO_4 is scavenged and decomposes to HNO_2 and O_2 in the aqueous phase [Park and Lee, 1987]. This aqueous-phase sink is faster than gas-phase thermal decomposition so that HNO_4 concentrations are a factor of 3 lower in the cloud than below. By contrast, OH and HO_2 concentrations are higher in the cloud because of the stronger radiation intensities (which enhance odd hydrogen production).

Figure 11 summarizes the cycling of odd hydrogen species in the cloud. We find that scavenging by cloud droplets contributes only a minor sink to the budgets of gas-phase OH and HO_2. This result is in stark contrast with model calculations of clouds in low-NO_x atmospheres, where scavenging by cloud droplets is the main sink of HO_2 [Chameides and Davis, 1982; Schwartz, 1984; Jacob, 1986]. Under the high-NO_x conditions simulated here, the gas-phase reaction of HO_2 with NO is fast compared to scavenging.

Cloud water concentrations of OH and $O_2(-I)$ in Figure 11 are 1 to 2 orders of magnitude lower than values predicted for tropical clouds [Chameides and Davis, 1982; Jacob, 1986]. The depletion of $O_2(-I)$ follows in part from the depletion of gas-phase HO_2 and in part from the rapid aqueous-phase reactions of $O_2(-I)$ with metal ions. The depletion of OH is due mainly to the abundance of $H_2C(OH)_2$ (hydrated formaldehyde), since $O_2(-I)$ produced from the reaction $H_2C(OH)_2$ + OH reacts with metal ions and is not recycled back to OH (Figure 11). In contrast, the reaction S(IV) + OH is not an efficient sink for OH because OH is recovered by the reaction Cl + H_2O in the subsequent oxidation chain (see section 4).

Concentrations of H_2O_2 in the boundary layer range from 2 to 5 ppt at noon and from 10 to 20 ppt at midnight; these low values

are due to depletion of the precursors HO_2 and $O_2(-I)$, and to the rapid reaction of H_2O_2 with S(IV) in the aqueous phase. The diurnal variation of H_2O_2 concentrations is largely controlled by the rate of the S(IV) + Fe(III) reaction, which provides the main H_2O_2 source. At noon, production of H_2O_2 from $O_2(-I)$ reduction by metal ions is comparable to production from the S(IV) + Fe(III) reaction (Figure 11), but the latter source is much faster at night when the cloud water pH is higher (section 4).

3.4. Sulfur(IV)

The simulated S(IV) cloud water concentrations on model day 3 range from 72 μM to 547 μM; the mean liquid water-weighted concentration is 131 μM. By comparison, the cloud water concentrations observed at McKittrick on January 3-5, 1984, ranged from 14 to 95 μM [Jacob, 1985], lower than predicted. Higher concentrations were observed in Bakersfield fogs sampled at other times during the January 1984 experiment (mean [S(IV)] = 384 μM; JMWH). Cloud water concentrations of S(IV) are strongly dependent on liquid water content and pH [Olson and Hoffmann, 1989]; therefore simulation of observations is difficult. The fact that the simulated and observed values are within 1 order of magnitude suggests that the simulation may be reasonable.

We show in Figure 12 the time evolution of S(IV) concentrations in layer 6 (375 m AGL). Over 90% of total S(IV) is present as S(IV)-carbonyl complexes, with HMS by far the most abundant. This result is in harmony with the observation by Munger et al. [1986] that HMS is the main S(IV) species present in Bakersfield fog samples. Formation of HMS in the model is facilitated by the abundance of the precursor CH_2O, which accumulates quickly to a steady concentration of 7 ppb and is not depleted at night because of continuous supply from direct emissions. The CH_2O concentrations predicted by the model are consistent with the mean Bakersfield value of 10 ppb reported by Munger et al. [1989] on the basis of simultaneous measurements of fog water CH_2O concentrations and liquid water contents.

The HMS concentrations in the model increase rapidly at night and decrease slowly during the day (Figure 12). This pattern reflects mainly the enhanced production of HMS at night. The main source of HMS is the reaction of CH_2O with SO_3^{2-}:

(R3) $CH_2O + SO_3^{2-} \rightarrow {}^-OCH_2SO_3^-$

followed by

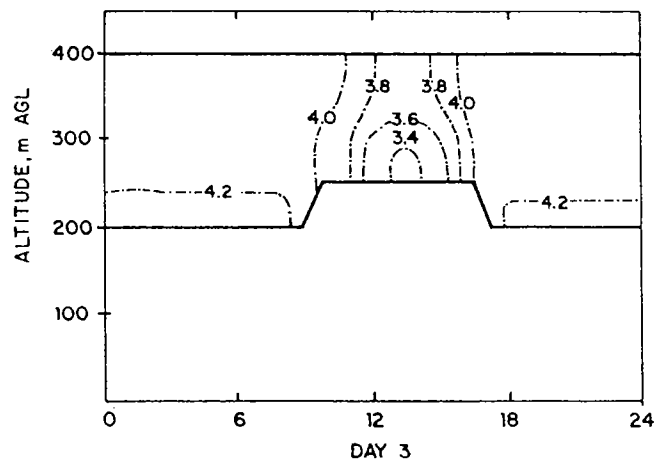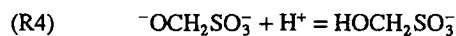(R4) ${}^-OCH_2SO_3^- + H^+ = HOCH_2SO_3^-$
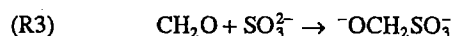
Fig. 9. Cloud water pH as a function of altitude and time of day on model day 3. The thick line is the cloud boundary.
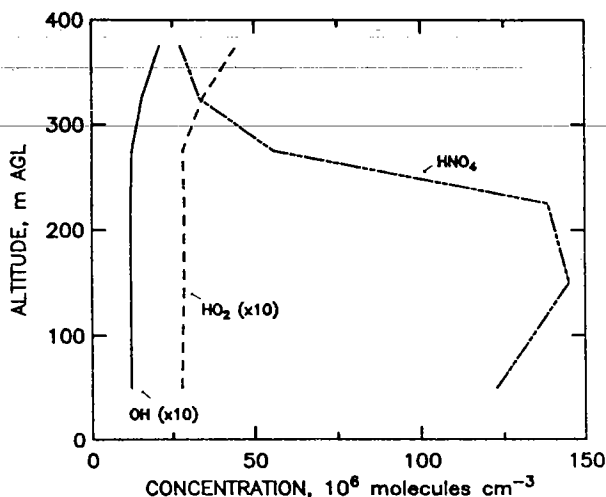
Fig. 10. Vertical profiles of gas-phase OH, HO_2, and HNO_4 concentrations on model day 3 at noon.

Cloud water pH values are higher at night; hence SO_3^{2-} concentrations are higher and HMS production is faster. The progressive accumulation of HMS over the course of the stagnation episode reflects the inefficiency of the HMS removal processes (ventilation, deposition, aqueous-phase oxidation by OH), which all have time scales of several days. The slow rate of HMS oxidation in the Bakersfield atmosphere contrasts with tropical clouds where aqueous-phase OH concentrations are much higher and the lifetime of HMS against oxidation may be less than 1 hour at noon [*Jacob*, 1986; *Martin et al.*, 1989].

The other S(IV)-carbonyl complexes (HAMS, GMBS, GDBS) are less abundant than HMS, reflecting, in part, the relatively low

model concentrations of methylglyoxal (0.1-0.3 ppb) and glyoxal (0.1-0.4 ppb) compared to CH_2O. Another contributing factor is that the thermal dissociation reactions of HAMS, GMBS, and GDBS are relatively rapid. For example, HAMS has a lifetime of 1 hour against thermal dissociation at pH 4 and 6°C, compared to 150 days for HMS (cf. data in Table 3). The rapid nighttime decay of HAMS in the simulation (Figure 12) is caused by thermal dissociation following the removal of methylglyoxal by deposition.

4. SO$_2$ OXIDATION MECHANISMS

The contributions to S(VI) production from individual SO_2 oxidants are shown in Figure 13 for model day 3. Four mechanisms make significant contributions: (1) aqueous-phase autoxidation catalyzed by Fe(III), (2) aqueous-phase oxidation by H_2O_2, (3) gas-phase oxidation by OH, and (4) aqueous-phase oxidation by OH (including the ensuing S(IV) oxidation chain). Other aqueous-phase SO_2 oxidants such as Mn(II), O_3, CH_3OOH, $CH_3C(O)COOH$, and $O_2(-I)$ are negligible. The contribution from H_2O_2 follows closely that from Fe(III) because the main source of H_2O_2 is the S(IV) + Fe(III) reaction. In this section we examine the various factors controlling S(VI) production by the aqueous-phase reactions S(IV) + Fe(III) and S(IV) + OH.

4.1. S(IV) + Fe(III)

Sulfate production by the S(IV) + Fe(III) reaction is much faster at night than in the daytime (Figure 13), due mainly to the diurnal variation of pH and hence of the cloud water concentration of SO_3^{2-}, the reactive S(IV) species. The cloud water concentrations of Fe(III) are higher in the daytime than at night because of the lower liquid water content, but this effect is canceled when sulfate
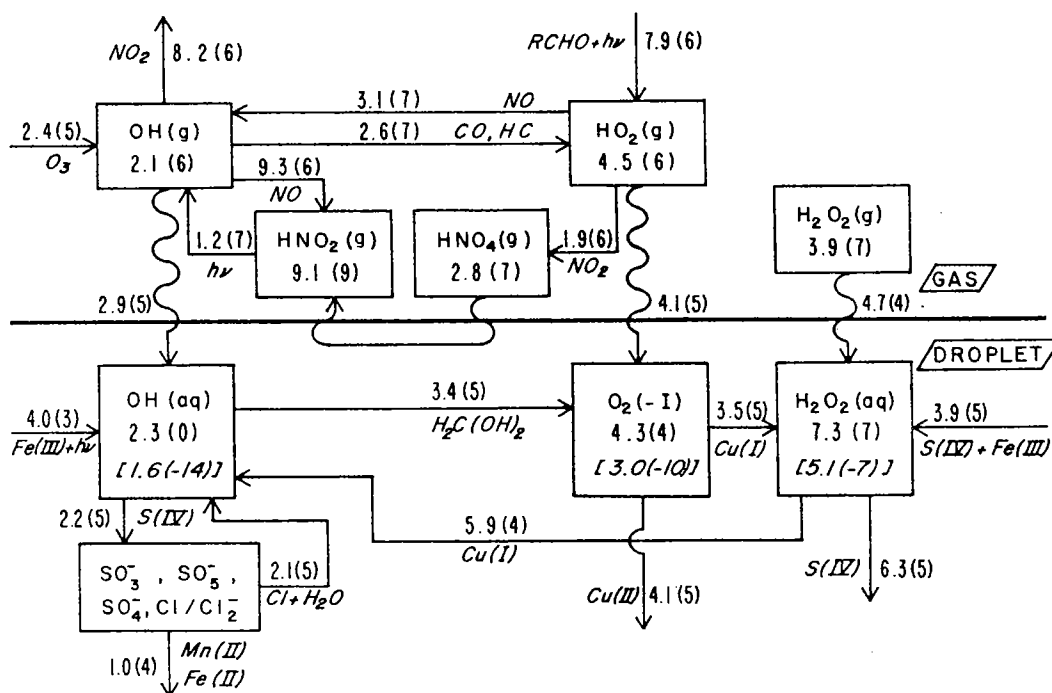

Fig. 11. The odd hydrogen cycle in cloud (layer 6, model day 3 at noon). The main reaction pathways are indicated. Concentrations are in units of molecules per cubic centimeter of air, and transformation rates are in units of molecules per cubic centimeter of air per second. Aqueous-phase concentrations (*M*) are given in brackets. Organic peroxy radicals are not shown explicitly; under the high-NO$_x$ conditions simulated here, they react mainly with NO to eventually yield HO_2.
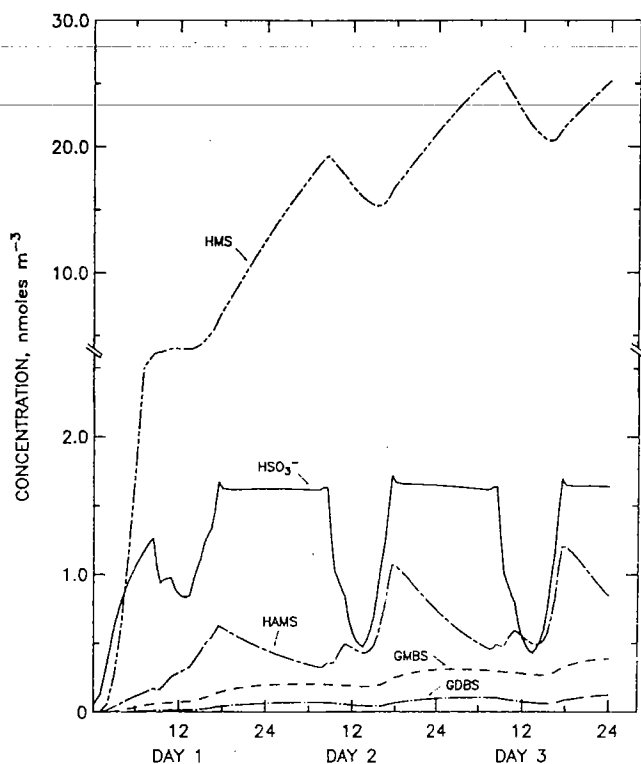
Fig. 12. Time evolution of simulated S(IV) concentrations in layer 6. Note the discontinuity in the ordinate scale.

production per unit volume of air is considered as in Figure 13. The Fe(II)/Fe(III) ratio shows little diurnal variation (Figure 14a).

The partitioning of iron between its two oxidation states in the model is largely controlled by the respective reactivities of Fe(II) and Fe(III) with O_2(-I) (Figure 14a). Oxidation of Fe(II) by O_2 is negligibly slow in the range of pH values found in cloud water [Sung and Morgan, 1980]. We find that most of the soluble iron is present as Fe(II); only a small fraction (10-15%) is present as Fe(III). This result is in contradiction with the raindrop chemistry model calculations of Graedel et al. [1986] in which Fe(III) was found to contribute 90% of total dissolved iron. The main reason for the contradiction is that Graedel et al. [1986] used for the Fe(II) + O_2^- reaction a rate constant of 8.7×10^8 M^{-1} s^{-1} which was indirectly inferred by Matthews [1983] to explain an observed nonlinearity in the Fe(III) yield from the irradiation of $FeSO_4$ solutions at various concentrations. Since then the rate constant for the Fe(II) + O_2^- reaction has been directly measured [Rush and Bielski, 1985] and found to be 80 times higher than the value given by Matthews [1983]. If Fe(II) is indeed the most abundant oxidation state of soluble iron in cloud water, as we argue here, then the cloud chemistry models based on the assumption that soluble iron is Fe(III) [Jacob and Hoffmann, 1983; Seigneur and Saxena, 1984] would seriously overestimate S(VI) production rates.

We conducted a sensitivity calculation in which the radical mechanism for the S(IV) + Fe(III) reaction was assumed, i.e., stoichiometry (R1) was replaced by stoichiometry (R2) in the chemistry code. The simulated S(IV) and S(VI) concentrations are shown in Figure 15. The concentrations of S(VI) are much lower than with the nonradical mechanism; by contrast, S(IV) accumulates to high levels. The S(IV) + Fe(III) reaction by the radical mechanism is the main sink for Fe(III), and is therefore self-inhibiting because of Fe(III) depletion (Figure 14b). The rate of

the S(IV) + Fe(III) reaction is limited by the rate of Fe(II) oxidation, which is slow due to the scarcity of radical oxidants. At night the production of S(VI) is insignificant, so that cloud water pH is maintained at a relatively high level (~5.0) which allows efficient production of HMS. After 3 model days, HMS contributes 70% of total aerosol sulfur (in equivalent units).

Although the nonradical and radical mechanisms predict very different S(VI) concentrations, one cannot discriminate between the two on the basis of S(VI) aerosol concentration measurements, because S(IV) was not preserved in the aerosol samples and therefore could have been oxidized to S(VI) during the interval between sample collection and analysis. A more reliable diagnostic is the measured S(IV)/S(VI) equivalent ratio in cloud water, since S(IV) was preserved in cloud water samples immediately upon collection (JMWH). The measured S(IV)/S(VI) ratios in the stratus clouds sampled at McKittrick were always less than 0.2, and in Bakersfield fog water they were less than 0.5 in 80% of the samples [Jacob, 1985]. These observations lend support to the non-radical mechanism.

4.2. $S(IV) + OH$

Aqueous-phase oxidation of S(IV) by OH initiates a chain reaction propagated by reactions of S(IV) with the radicals SO_5^-, SO_4^-, and Cl_2^- [McElroy, 1986b]. A major uncertainty in assessing the chain length under atmospheric conditions is that the reactivity of HMS with the radical intermediates is unknown. We have assumed here that the S(IV)-carbonyl adducts do not react with SO_5^-, SO_4^-, or Cl_2^-, so that only HSO_3^- is involved in chain propagation. The main steps of the reaction sequence, and their rates, are listed in Table 5. The chain is initiated by

(R5) $S(IV) + OH \rightarrow SO_3^- + H_2O + products$
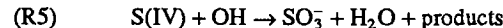
where it is assumed that oxidation of S(IV)-carbonyl adducts produces the SO_3^- radical. Reaction (R5) is followed by rapid addition of O_2 to SO_3^- [Huie and Neta, 1984]:

(R6) $SO_3^- + O_2 \rightarrow SO_5^-$
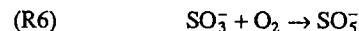
The main sinks of SO_5^- in atmospheric clouds are expected to be the reactions with O_2^-, $HCOO^-$, and SO_5^- [Jacob, 1986; Huie and Neta, 1987]. Reaction with HSO_3^- is slow [Huie and Neta, 1987].
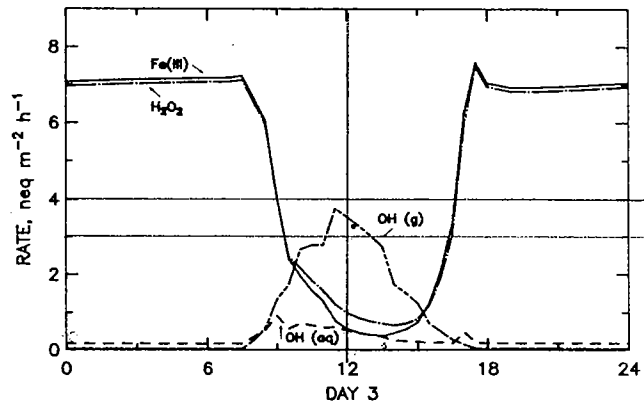

Fig. 13. Contributions of individual SO_2 oxidants to S(VI) production on model day 3, as a function of time of day. Results are shown as column rates of S(VI) production integrated over the depth of the boundary layer.
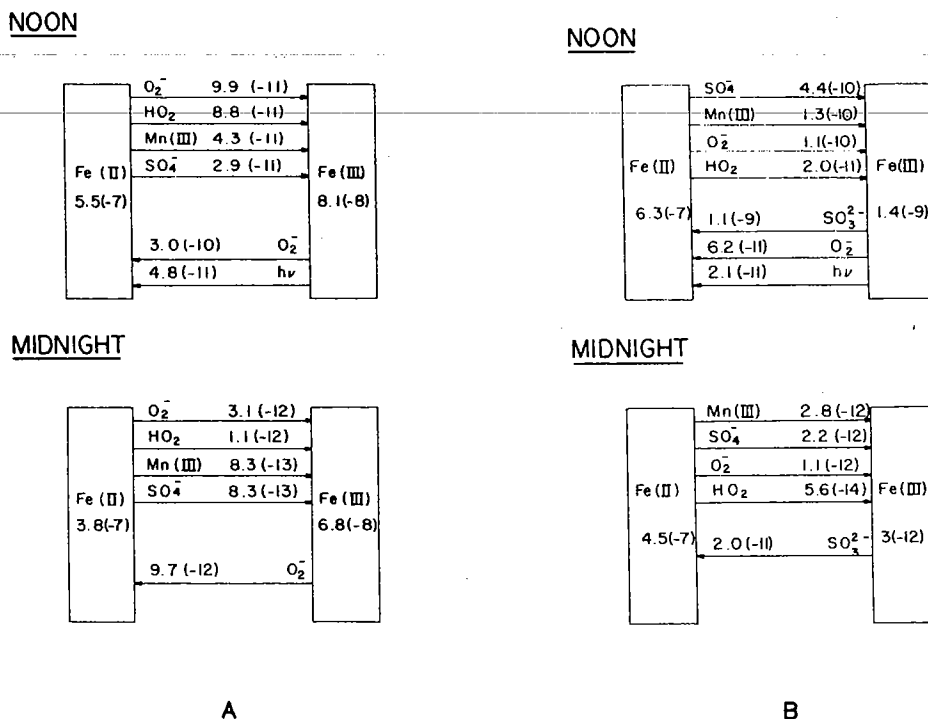
Fig. 14. Cycling of soluble iron between Fe(II) and Fe(III) in the simulation, assuming (a) the non-radical mechanism for the reaction S(IV) + Fe(III) (standard simulation), and (b) the radical mechanism. The values shown are average cloud water concentrations (M) and transformation rates $(M\ s^{-1})$ on model day 3 at noon and at midnight. The averages are computed by integration over the depth of the cloud (250 to 400 m at noon, 187.5 to 400 m at midnight).
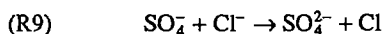
Under the high-sulfur conditions simulated here, the self-reaction is dominant:

(R7) $SO_5^- + SO_5^- \rightarrow 2SO_4^- + O_2$
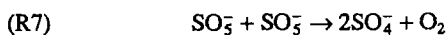
The sulfate radical produced by (R7) reacts rapidly with most reduced species. Reaction with HSO_3^- would complete the propagation cycle:

(R8) $SO_4^- + HSO_3^- \rightarrow SO_3^- + H^+ + SO_4^{2-}$
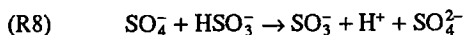
However, Cl^- is more abundant than HSO_3^-, so that (R9) dominates over (R8):

(R9) $SO_4^- + Cl^- \rightarrow SO_4^{2-} + Cl$

(R10) $Cl + Cl^- = Cl_2^-$

Reaction (R9) produces the Cl/Cl_2^- radical, which is mainly present as Cl_2^- at the Cl^- concentrations simulated here. Reaction of Cl_2^- with HSO_3^- would again complete the propagation cycle:

(R11) $HSO_3^- + Cl_2^- \rightarrow SO_3^- + 2Cl^- + H^+$
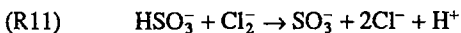
However, recent kinetic studies [*Wine et al.*, 1988; *McElroy*, 1988] indicate that the reaction of Cl with H_2O is sufficiently fast to compete with (R11):

(R12) $Cl + H_2O \rightarrow Cl^- + H^+ + OH$
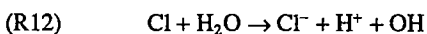
Wine et al. [1988] report a preliminary rate constant of $1 \times 10^5\ s^{-1}$ for (R12); they find by contrast that the reaction $Cl_2^- + H_2O$ is very slow. Under our model conditions, the reaction $Cl + H_2O$ effectively prevents propagation of the chain (Table 5). As a result the S(VI) yield is little more than unity, and the S(IV) + OH reaction is only a minor contributor to total S(VI) production.

Efficient propagation of the reaction chain could, however, occur at different HSO_3^- and Cl^- concentration regimes. From the mechanism of Table 5 we derive an analytical expression for the S(VI) yield as a function of droplet composition:

$$S(VI)\ \text{yield} = \frac{1}{1-A} \qquad (6)$$

with

$$A = \frac{k_{11}[HSO_3^-]}{k_{11}[HSO_3^-]+k_{16}[NO_2^-]+k_{12}/(K_{10}[Cl^-])} \cdot \frac{k_9[Cl^-]}{B} + \frac{k_8[HSO_3^-]}{B}$$

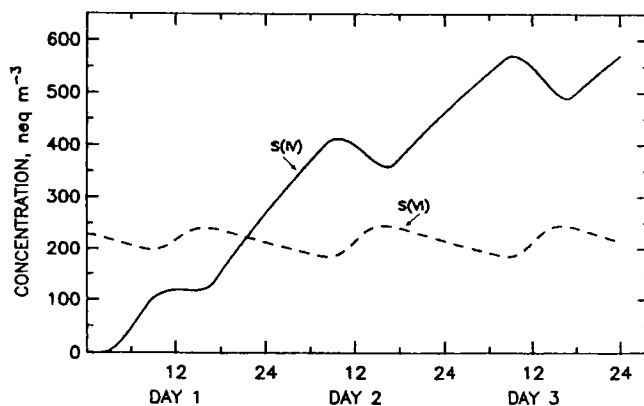$$B = k_8[HSO_3^-]+k_9[Cl^-]+k_{13}[Mn(II)]+k_{14}[Fe(II)] + k_{15}$$

Fig. 15. Time evolution of simulated S(IV) and S(VI) concentrations in layer 1, assuming the radical mechanism for the S(IV) + Fe(III) reaction.

TABLE 5. Radical-assisted chain oxidation of S(IV)

Reaction	Rate, $M\ s^{-1}$

Initation

(R5a)	$HMS + OH \rightarrow SO_3^- + CH_2O + H_2O$	1.4(-9)
(R5b)	$HSO_3^- + OH \rightarrow SO_3^- + H_2O$	1.2(-10)
(R5c)	$HAMS + OH \rightarrow MGLYA + SO_3^- + H_2O$	3.4(-11)
(R5d)	$GMBS + OH \rightarrow GLYXA + SO_3^- + H_2O$	1.7(-11)

Propagation

(R6)	$SO_3^- + O_2 \rightarrow SO_5^-$	
(R7)	$SO_5^- + SO_5^- \rightarrow 2SO_4^- + O_2$	8.3(-10)
(R8)	$SO_4^- + HSO_3^- \rightarrow SO_4^{2-} + SO_3^- + H^+$	8.3(-11)
(R9)	$SO_4^- + Cl^- \rightarrow SO_4^{2-} + Cl$	1.7(-9)
(R10)	$Cl + Cl^- = Cl_2^-$	
(R11)	$HSO_3^- + Cl_2^- \rightarrow SO_3^- + 2Cl^- + H^+$	1.7(-10)

Termination

(R12)	$Cl + H_2O \rightarrow Cl^- + H^+ + OH$	1.5(-9)
(R13)	$SO_4^- + Mn(II) \rightarrow SO_4^{2-} + Mn(III)$	2.9(-11)
(R14)	$SO_4^- + Fe(II) \rightarrow SO_4^{2-} + Fe(III)$	2.6(-11)
(R15)	$SO_4^- + H_2O \rightarrow SO_4^{2-} + H^+ + OH$	2.4(-11)
(R16)	$Cl_2^- + NO_2^- \rightarrow 2Cl^- + NO_2$	7.6(-12)

Rates are for 375 m AGL at noon. Read 1.4(-9) as 1.4×10^{-9}. Concentrations are $[SO_5^-] = 1.4\times10^{-9}\ M$; $[SO_4^-] = 6.6\times10^{-14}\ M$; $[Cl] + [Cl_2^-] = 3.2\times10^{-13}\ M$; $[HSO_3^-] = 2.3\times10^{-6}\ M$; $[Cl^-] = 1.1\times10^{-4}\ M$; $[Mn(II)] = 3.5\times10^{-8}\ M$; $[Fe(II)] = 5.5\times10^{-7}\ M$; $[NO_2^-] = 1.4\times10^{-7}\ M$.

where we have defined the S(VI) yield as the number of S(VI) molecules produced per individual reaction S(IV)+OH. The yield computed from equation (6) is plotted in Figure 16 as a function of $[HSO_3^-]$ and $[Cl^-]$, with concentrations of other species fixed at their values from the standard simulation. The yield increases linearly with $[HSO_3^-]$ for $[HSO_3^-] > 1\ \mu M$, but the dependence on $[Cl^-]$ is more complicated. In the limit of low $[Cl^-]$ the reaction $SO_4^- + Cl^-$ is unimportant, and the yield is therefore independent of $[Cl^-]$. As $[Cl^-]$ increases, the reaction $SO_4^- + Cl^-$ becomes the major loss mechanism for SO_4^-, leading to chain termination by the reaction $Cl + H_2O$. However, an increase of $[Cl^-]$ also decreases $[Cl]$ by shifting the Cl/Cl_2^- equilibrium toward Cl_2^-; eventually at high $[Cl^-]$, reaction (R11) dominates (R12), and the chain is efficiently propagated. A minimum in the S(VI) yield is found for $[Cl^-]$ of the order of $10^{-4}\ M$. The conditions of the Bakersfield simulation happen to coincide with this minimum (Figure 16).

Inspection of Figure 16 suggests that high S(VI) yields could be achieved when $[HSO_3^-] > 10^{-5}\ M$. Bisulfite concentrations of this magnitude require an unusual combination of high SO_2 concentration and high pH [*Munger et al.*, 1984]. However, equation (6) relies on the assumption that HSO_3^- is the only S(IV) species involved in the chain-propagating reactions with SO_4^- and Cl_2^-; the S(VI) yields could be much higher if S(IV)-carbonyl adducts were involved in chain propagation. For example, if we assume that all S(IV) species react with SO_4^- and Cl_2^- at the same rate as HSO_3^- (and give identical sulfur radical products), then [S(IV)] should replace $[HSO_3^-]$ as the ordinate in Figure 16. Total S(IV) cloud wa-

ter concentrations in excess of $10^{-5}\ M$ are observed routinely in polluted fogs and stratus clouds [*Richards et al.*, 1983; *Munger et al.*, 1984], so that high S(VI) yields would occur over a broad range of conditions. Another regime where high S(VI) yields would be expected is for $[Cl^-] > 10^{-3}\ M$ (Figure 16). Such Cl^- concentrations are commonly found in coastal fogs and stratus [*Jacob et al.*, 1985; *Munger*, 1989] and have also been observed in highly polluted fogs near Zurich, Switzerland [*Johnson et al.*, 1987].

5. DISCUSSION

5.1. *Control of Sulfate Production by Ammonia*

Table 6 summarizes the results from a number of sensitivity simulations in which we investigated the effects of changes in model conditions on model results. A remarkable feature common to all simulations is the close balance between concentrations of acids and bases; in all cases, the atmospheric alkalinities are small compared to the total concentrations of acids or bases. We also find that the predicted S(VI) concentrations are largely insensitive to changes in SO_2 emissions, NO_x emissions, cloud liquid water content, or trace metal concentrations. By contrast they vary almost linearly with NH_3 emissions and are strongly dependent on the boundary layer ventilation rate.

It appears from Table 6 that the sensitivity of S(VI) concentrations to changes in model conditions reflects mainly the effect of these changes on the N(-III) concentrations. The reason for this behavior is that S(VI) production by the S(IV) + Fe(III) reaction is controlled by the availability of NH_3. The S(IV) + Fe(III) reaction adds acidity to the droplet and is self-limiting unless NH_3 is available to neutralize the acidity; continuous supply of NH_3 from fresh emissions sustains a matching production of S(VI), but once NH_3 is exhausted, a small increase in S(VI) causes a rapid drop in cloud water pH which quenches further S(VI) production. The NH_3 concentrations simulated by the model (>1000 neq m^{-3}) are much higher than the free acidities needed to quench the S(IV) + Fe(III) reaction in cloud (10-100 neq m^{-3}), so that the total concentration of acids in cloud is only slightly in excess of the N(-III) concentration. At ground level we find that N(-III) is in slight excess (Table 6) because of the proximity of the NH_3 source.
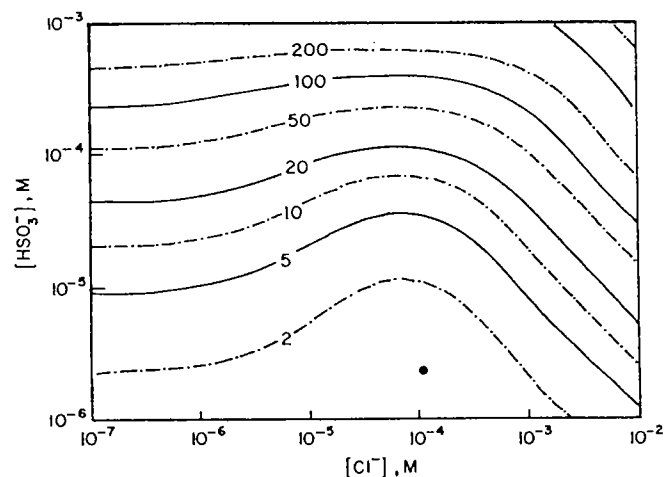

Fig. 16. Sulfate yield of the radical-assisted S(IV) oxidation chain as a function of $[HSO_3^-]$ and $[Cl^-]$, with other conditions as in Table 5. The yield is computed from equation (6). The dot indicates the conditions of the standard Bakersfield simulation.

TABLE 6a. Summary of Results From Sensitivity Runs:
Concentrations in Layer 1, Model Day 3 at Midnight

	S(VI)	S(IV)	N(V)	N(-III)	ALK
Observations	855		395	1196	-54±281[a]
Standard model	771	26	347	1207	63
Liquid water content/2	735	10	380	1194	69
10% metals soluble[b]	701	78	345	1196	72
No ventilation	1288	48	671	2070	63
SO$_2$ emissions/2	743	28	347	1187	69
NH$_3$ emissions/2	354	10	317	695	14
NO$_x$ emissions/2	840	28	266	1198	64

Concentrations are in units of neq m^{-3}.

[a] Expected value ± uncertainty; the uncertainty on the measured value of (ALK) is large because the individual uncertainties on the measurements of (S(VI)), (N(V)), and (N(-III)) are compounded (see JMWH).

[b] As compared to 30% in the standard simulation.

It follows from the above discussion that a close balance between acids and bases should be a general characteristic of highly polluted atmospheres where aqueous-phase oxidation of SO$_2$ is the main source of acidity. Indeed, the fact that such a balance is systematically observed at Bakersfield can be taken as indirect evidence that the oxidation of SO$_2$ proceeds by an aqueous-phase mechanism whose rate decreases with decreasing pH. The frequently observed correlation between [SO$_4^{2-}$] and [NH$_4^+$] in precipitation over polluted regions [Schuurkes et al., 1988] can also be explained in this manner. Control of S(VI) production by NH$_3$ may further explain the observation that S(VI) aerosol tends to be neutral in cities and acidic in rural environments [Koutrakis et al., 1988; P. Koutrakis, Harvard School of Public Health, personal communication, 1988].

5.2. Cloud Water pH

The cloud water pH at night is controlled by a balance between the reaction S(IV) + Fe(III) (which is the main source of acidity) and NH$_3$ emission. Because the rate of the S(IV) + Fe(III) reaction is strongly dependent on cloud water pH, a steady state pH is approached where the rate of acid production equals the rate of NH$_3$ emission. An approximate analytical expression for this steady state can be obtained using a simplified box model with the following assumptions: (1) the cloud is of uniform composition, (2) transport within the boundary layer is rapid, and (3) SO$_2$ levels are controlled by emission and deposition. The balance between

Table 6b. Summary of Results From Sensitivity Runs:
Cloudwater Acidities in Layer 6, Model Day 3 at
Noon and Midnight

	[H$^+$], μM		pH	
	Noon	Midnight	Noon	midnight
Standard model	152	72	3.82	4.14
Liquid water content/2	270	86	3.57	4.07
10% metals soluble	116	45	3.94	4.35
No ventilation	217	84	3.66	4.08
SO$_2$ emissions/2	96	49	4.02	4.31
NH$_3$ emissions/2	323	98	3.49	4.01
NO$_x$ emissions/2	105	66	3.98	4.18

S(VI) production and NH$_3$ emission is then expressed as follows:

$$\frac{2kK_HK_{a1}K_{a2}RT}{V_d[\text{H}^+]^2}(\text{Fe(III)})\text{E}_{\text{SO2}} = \frac{\text{E}_{\text{NH3}}}{z_T} \quad (7)$$

where k (M^{-1} s^{-1}) is the aqueous-phase rate constant of the S(IV) + Fe(III) reaction; K_H (M atm^{-1}), K_{a1} (M), and K_{a2} (M) are the Henry's law and acid dissociation constants for SO$_2$; R (atm cm^3 mol^{-1} K^{-1}) is the ideal gas constant; T (degrees Kelvin) is the temperature; V_d (centimeters per second) is the SO$_2$ deposition velocity; (Fe(III)) is the Fe(III) concentration in moles per cubic centimeter of air; E$_{\text{NH3}}$ and E$_{\text{SO2}}$ (molecules per square centimeter per second) are emission rates of NH$_3$ and SO$_2$, respectively; and z_T (centimeters) is the thickness of the boundary layer. Rearrangement of equation (7) yields an expression for the steady state [H$^+$]:

$$[\text{H}^+] = \left[\frac{2kK_HK_{a1}K_{a2}RTz_T}{V_d}(\text{Fe(III)})\frac{\text{E}_{\text{SO2}}}{\text{E}_{\text{NH3}}}\right]^{1/2} \quad (8)$$

The dependence of [H$^+$] on [E$_{\text{SO2}}$/E$_{\text{NH3}}$]$^{1/2}$ in equation (8) implies that the cloud water pH should be only moderately sensitive
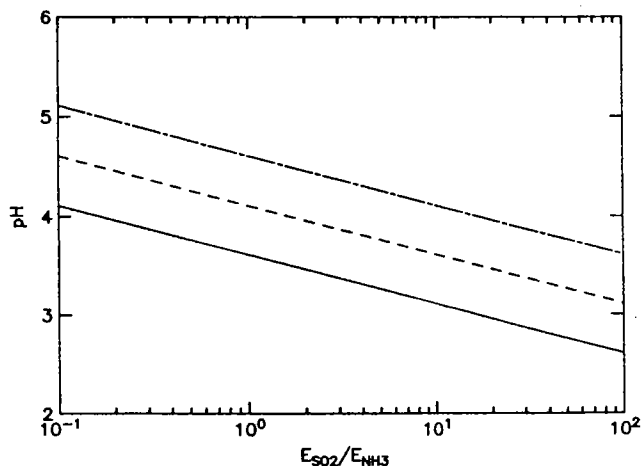

Fig. 17. Steady state nighttime cloud water pH computed from equation (8) as a function of E$_{\text{SO2}}$/E$_{\text{NH3}}$, with $T = 6°C$, $V_d = 1$ cm s^{-1}, and $z_T = 400$ m. Results are shown for (Fe(III)) = 1 nmol m^{-3} (solid line), 0.1 nmol m^{-3} (dashed line), and 0.01 nmol m^{-3} (dot-dash line).
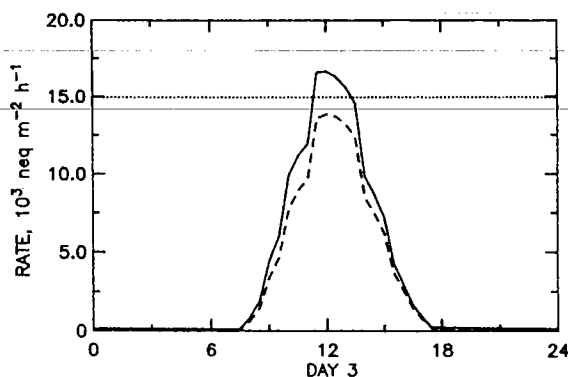
Fig. 18. Gas-phase production of acidity as a function of time of day on model day 3. Results are shown as column rates integrated over the depth of the boundary layer. The solid line is the total acid production rate from the reactions $NO_2 + OH$ and $SO_2 + OH$ (the latter reaction produces two equivalents of acidity). The dashed line is the contribution from $NO_2 + OH$ alone. The dotted line is the NH_3 emission rate.

to changes in SO_2 or NH_3 emissions. The dependence on z_T does not necessarily mean that an increase in mixed layer depth would decrease the cloud water pH since such an increase would also tend to decrease the Fe(III) concentration by dilution. We plot in Figure 17 the steady state cloud water pH as a function of (E_{SO2}/E_{NH3}) and (Fe(III)), for $T=6°C$, $V_d = 1$ cm s^{-1}, and $z_T = 400$ m. Under the conditions of the standard simulation, equation (8) yields $pH = 4.23$ ($E_{SO2}/E_{NH3} = 2.5$, (Fe(III)) $= 2.3 \times 10^{-17}$ mol cm^{-3}), which compares fairly well with the value of 4.14 computed for layer 6 at midnight in the complete model. The assumption that the boundary layer is well mixed causes a small underestimate of the acidity (cf. Figure 8). The results in Figure 17 demonstrate that highly acidic clouds would not occur in the Bakersfield atmosphere at night even if SO_2 emissions increased drastically.

The lower pH values in the daytime than at night are due to additional acid input from the photochemical gas-phase reactions $NO_2 + OH$ and $SO_2 + OH$. We plot in Figure 18 the gas-phase acid production rate integrated over the depth of the boundary layer, in the standard simulation, as a function of time of day; the diurnal variation of this rate essentially follows that of the OH concentration. As long as NH_3 emissions (superimposed on Figure 18 for comparison) exceed the gas-phase acid production rate, the cloud water pH can still be described approximately by a steady state between the reaction S(IV) + Fe(III) and the available excess NH_3. This steady state pH decreases as the morning progresses and NH_3 is increasingly depleted by the growing acid input. Eventually at midday the gas-phase acid production rate exceeds the rate of NH_3 emissions, and acidity accumulates in the boundary layer, causing a rapid pH drop, particularly in the bottom portion of the cloud where the liquid water content is lowest (Figure 9). This regime of excess acid production is maintained only for about 2 hours, until 1330 local time; at that time the cloud water pH has reached its minimum value and begins to rise again in response to the excess input of NH_3. By late afternoon the cloud water pH is back at a value approaching the nighttime steady state.

From the above discussion it appears that extremely high acidities in the Bakersfield atmosphere may be attained only during the daytime hours when gas-phase acid production by the reactions $NO_2 + OH$ and $SO_2 + OH$ exceeds NH_3 emissions. The cloud water acidities predicted by the model in the daytime are more sensitive to model conditions than at night, as shown in Table 6;

changes in emissions of NH_3, SO_2, or NO_x directly alter the magnitude of the excess acidity and thus have a strong effect on cloud water pH. Variations in cloud liquid water content also affect pH in the daytime by changing the amount of water into which the excess acidity is dissolved. The radiation field plays an important role in determining the daytime acid production rates because the OH concentrations scale almost linearly to the radiation intensities. Accurate representation of the radiation field in and below cloud is therefore a critical element in the simulation of acid production in polluted cloudy boundary layers.

6. CONCLUSIONS

We have developed a detailed photochemical model which simulates successfully the main features of the chemical evolution observed during a wintertime stagnation episode with low stratus in Bakersfield, California. A remarkable feature of the observations is the close balance maintained at all times between total atmospheric concentrations of acids and bases. We argue that this balance is evidence that the production of H_2SO_4 (the principal contributor to the acidity) proceeds by an aqueous-phase SO_2 oxidation mechanism whose rate is inversely dependent on droplet acidity. The only mechanism in the model that provides a source of sulfate consistent with the observed sulfate accumulation pattern is the S(IV) + Fe(III) reaction, assuming that this reaction proceeds by a non radical mechanism in which Fe(III) acts as a catalyst for the autoxidation of S(IV). A radical mechanism for the S(IV) + Fe(III) reaction with Fe(II) and SO_3^- as immediate products is found to quench S(IV) oxidation because of depletion of Fe(III); this result follows from the absence of a rapid Fe(II) oxidation pathway in the model. The radical mechanism could possibly be an efficient source of sulfate if Fe(II) were oxidized to Fe(III) by a pathway not included in the model, e.g. the S(IV)-induced autoxidation reaction [Faust, 1985], or bacterial oxidation. Such pathways remain, however, hypothetical at this time. More laboratory studies of the mechanism of the S(IV) + Fe(III) reaction are needed.

Other aqueous-phase S(IV) oxidation mechanisms with rates inversely dependent on droplet acidity include the reactions with O_3 and OH. Very low concentrations of O_3 are observed in Bakersfield during wintertime stagnation episodes; therefore the S(IV) + O_3 reaction is negligible. The S(IV) + OH reaction initiates a S(IV) oxidation chain which would be a major source of sulfate if efficiently propagated. However, we find that chain propagation does not occur under our simulated conditions because of rapid termination by the reaction $SO_4^- + Cl^-$ followed by $Cl + H_2O$. Efficient propagation could take place under high-SO_2 conditions if the S(IV)-carbonyl adducts participate in the chain propagation steps, and also under high-Cl^- conditions (as in coastal fog and stratus). The model results point to the need for further kinetic information on the hydrolysis reactions of Cl and Cl_2^-, and for kinetic and product information on the reactions of S(IV)-carbonyl adducts with radical oxidants.

The inverse dependence of aqueous-phase SO_2 oxidation on cloud water acidity implies that sulfate production in the Bakersfield atmosphere (and in similar highly polluted environments) should be largely independent of SO_2 emissions and increase linearly with NH_3 emissions. Extremely high cloud water acidities ($pH < 3$) are unlikely to occur in such environments as a result of aqueous-phase SO_2 oxidation. High acidities may, however, be attained by other mechanisms, e.g., photochemical gas-phase acid production by the reactions $NO_2 + OH$ and $SO_2 + OH$.

TABLE A1. Optical Properties of the Cloud

| | Wavelength, nm | | |
	310	400	600
Photolysis	$O_3 \rightarrow O(^1D)$	NO_2	O_3 (Chappuis)
Mie			
Q_{ex}	2.062	2.077	2.097
Q_{ex}^*		1.09	
ω	0.999993	0.999999	0.999998
Atmosphere			
τ(Raleigh)			
Above cloud	0.90	0.27	0.054
Below cloud	0.10	0.03	0.006
τ(stratospheric ozone)	[0,1]	0	0
τ^*(cloud)		[0.1,2,4,8,16]	
ω	[0.98,1.00]	1	1

Brackets denote the set of different values for the cases.

APPENDIX: PHOTOLYSIS IN THE PRESENCE OF CLOUD

A1. Introduction

A new method of solving for the radiation field in an inhomogeneous, plane- parallel atmosphere with anisotropic scattering is presented. The technique is applicable to stratus clouds. It is based on the multistream method of *Feautrier* [1964] which has been extended to polarized Rayleigh scattering [*Prather*, 1974] and to anisotropic scattering by L. H. Auer and M. J. Prather (unpublished, see applications by *Cochran and Trafton* [1978] and *Logan et al.* [1981]). In this appendix we describe the physical properties of the cloud and relate them to the optical properties. The Mie phase function for the cloud is compared with the Henyey-Greenstein phase function. The method of solution is documented, and results for several atmospheric cases are presented.

A2. Physical Properties of the Cloud

The cloud is assumed to be a polydispersed gamma distribution $n(r)$ of spheres of pure H_2O with an effective radius $a = 10$ μm. We define X (units per cubic meter) to be the total concentration of drops, G (square meters) to be the average geometric cross section per droplet, and V (m^3 m^{-3}) to be the fractional volume occupied by the drops. The equations relating these quantities are then

$$\frac{d\ln[n(r)]}{d\ln[r]} = \frac{1}{b} - 3 - \frac{r}{ab} \qquad (A1)$$

where r is the droplet radius, $b = 0.15$ is a constant, and

$$X = \int_0^\infty n(r)\, dr \qquad (A2a)$$

$$G = \frac{\int_0^\infty \pi r^2 n(r) dr}{X} = 1.87 \times 10^{-10} \text{ m}^2 \qquad (A2b)$$

$$V = (4/3)a\, G\, X \qquad (A2c)$$

This distribution of drop sizes is typical of water clouds and gives a Mie scattering function that is moderately uniform with wavelength [see *Deirmendjian*, 1969]. The vertically integrated geometric cross section A of the cloud (dimensionless) is given by

$$A = \int_0^\infty G\, X\, dz = \frac{3 \times 10^{-6}}{4a} \int_0^\infty W dz \qquad (A3)$$

where W is the liquid water content in grams of liquid water per cubic meter of air ($W = 10^6 V$). In the Bakersfield simulation the total liquid water column in the daytime is 24 g m^{-2}; hence the vertically integrated geometric cross section is 1.8.

A3. Optical Properties of the Cloud

The optical properties of the cloud depend on wavelength and are derived from the distribution of droplet sizes and Mie scattering theory for spheres of pure H_2O [*Hansen and Travis*, 1974]. We use the Mie phase function for scattering of natural light, assuming that all light is unpolarized. A more complete treatment of scattering including polarization is not necessary for these conditions [*Prather*, 1974]. The cloud is assumed to be homogeneous and may therefore be described optically by a total extinction optical depth τ_{ex} (dimensionless), a single scattering albedo ω, and a scattering phase function P.

The optical depth for extinction (absorption plus scattering) of light is related to the geometric cross section by the efficiency factor Q_{ex} derived from Mie theory,

$$\tau_{ex} = Q_{ex}\, A \qquad (A4)$$

The factor Q_{ex} is approximately 2 for the combination of droplet sizes and wavelengths considered here and does not vary much over the wavelength range 300-600 nm, as shown in Table A1.

The single scattering albedo ω describes which fraction of extinction events results in scattering rather than absorption. For the visible wavelengths, water does not absorb significantly, less than 1 event in 10^5; and thus ω may be approximated as unity for clouds of modest optical depth.

The phase function $P(\cos\theta)$ defines the probability that scattered light will be deflected by an angle θ from its incident direction. The value of P is normalized such that integration over all solid angles (4π sr) is unity.

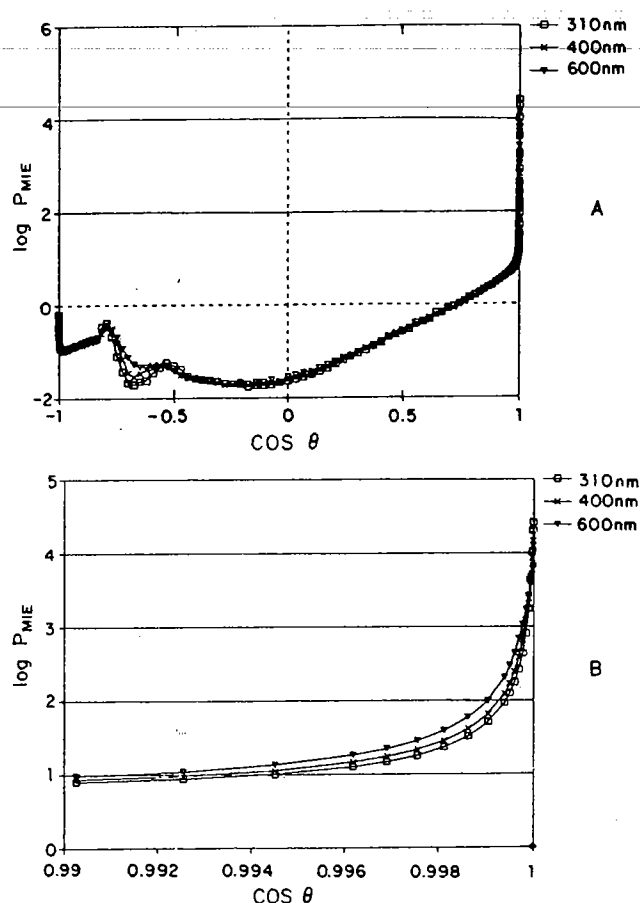$$\frac{1}{2} \int_{-\pi}^{+\pi} P(\cos\theta)\sin\theta d\theta = 1 \qquad (A5)$$

Fig. A1. Phase function for Mie scattering of spheres of pure H_2O with a Gamma distribution of effective radius 10 µm. The value of log P_{MIE} is plotted as a function of the cosine of the scattering angle, for three different wavelengths. (a) The full scale. (b) An expanded scale about the forward peak.

Mie phase functions for scattering of natural light are shown in Figure A1. From 300 to 600 nm, differences with wavelength are modest. The peaks in the phase functions correspond to the glory (180°), primary and secondary rainbows (142° and 122°), and the forward peak (0°, shown on an expanded scale in Figure A1b [see van de Hulst, 1981]). This forward peak is the most difficult part of the Mie phase function to model: it includes an extremely nonlinear response at small θ that is basically a diffraction pattern. For example, a black disk has an extinction efficiency $Q_{ex} = 2$, with absorption comprising half ($\omega = 0.5$) and scattering described by the diffraction pattern.

Anisotropic scattering by small particles is often approximated by the analytic Henyey-Greenstein phase function,

$$P_{HG}(\cos\theta) = \frac{1-g^2}{(1+g^2-2g\cos\theta)^{3/2}} \qquad (A6)$$

where the parameter g is a measure of the anisotropic forward peak. A comparison is made between a family of P_{HG} phase functions ($g = 0.8$ to 0.995) and P_{MIE} in Figure A2. While the Henyey-Greenstein phase function captures the essence of forward scattering, it does not adequately represent the shape of the Mie phase function.

Our solution of the scattering problem requires that the Mie phase function $P_{MIE}(\cos\theta)$ be decomposed into a Legendre series, but the forward diffraction peak cannot be adequately represented by an expansion of orthogonal polynomials in $\cos\theta$. The forward

peak results in very small scattering angles and may be treated as having merely passed the light through without scattering. Therefore we choose to truncate this forward peak by extrapolating log(P_{MIE}) linearly in $\cos\theta$ from 10° to 0°. This revised phase function is expanded in a Legendre series out to 80 terms and given in Table A2. The resulting phase functions-true Mie, truncated Mie, Legendre expansion-are compared in Figures A3 and A4 for the wavelength 400 nm. The Legendre expansion accurately reproduces the truncated Mie function to better than $10^{\pm0.04}$ over the range of P from 10^{-2} to 10^1, with the exception of the glory (not truncated like the forward peak) where errors are as large as $10^{-0.18}$.

Truncation of the forward peak reduces the effective scattering cross section and leads to a phase function that is not correctly normalized. The renormalized phase function P^* results in a value of Q_{ex}^* close to unity (see Table A1). Thus the cloud in the Bakersfield simulation has a renormalized extinction optical depth tex* equal to approximately 2 rather than 4. In the following we assume that all optical parameters have been renormalized and drop the asterisk notation.

A4. Solution of the Equation of Radiative Transfer

We present in this paper a new method of solving for anisotropic scattering by separating the even and odd parts of the radiation field and by solving the pair of differential equations that couple them. The equation of radiative transfer is solved for all orders of scattering in its integro differential form [Chandrasekhar, 1960]

$$\frac{\mu dI(\tau,\mu,\phi)}{d\tau} = I(\tau,\mu,\phi)$$

$$- \frac{\omega(\tau)}{4\pi}[\int_{-1}^{+1} d\mu' \int_0^{2\pi} d\phi' \, P(\tau,\mu,\phi,\mu',\phi')I(\tau,\mu',\phi')$$

$$- P(\tau,\mu,\phi,-\mu_o,\phi_o)\pi F_o e^{-\tau/\mu_o}] \qquad (A7)$$

In this notation, $I(\tau,\mu,\phi)$ is the specific intensity (photons cm^{-2} s^{-1} sr^{-1}) in the direction (μ,ϕ); the direction (μ,ϕ) refers to the cosine of the zenith angle (e.g., $\mu = +1$ points upward) and the azimuthal angle, respectively; τ is the vertical optical depth, nominally zero at the top of the atmosphere; ω is the single scattering albedo; $P(\tau,\mu,\phi,\mu',\phi')$ is the phase function at optical depth τ for scattering by an angle

$$\cos\theta = \mu\mu' + (1-\mu^2)^{1/2}(1-\mu'^2)^{1/2}\cos(\phi - \phi') \qquad (A8)$$
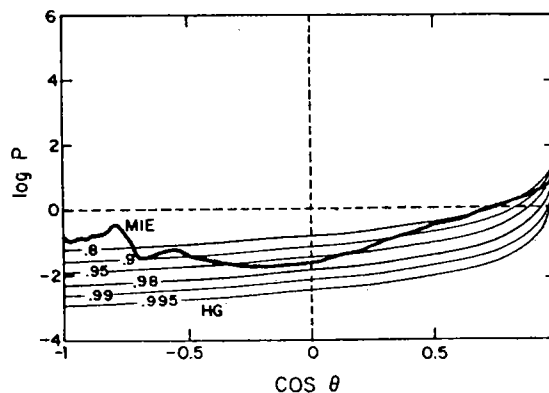

Fig. A2. Phase function for scattering of spheres of pure H_2O with a gamma distribution of effective radius 10 µm. The value of log P is plotted as a function of the cosine of the scattering angle. The Mie phase function at 400 nm is compared to a family of Henyey-Greenstein phase functions ($g = 0.8$ to 0.995).

TABLE A2. Legendre Expansion Coefficients to Mie Phase Function at 400 nm

l	ω_l	l	ω_l	l	ω_l	l	ω_l
0	1.	20	0.159261	40	0.010299	60	-0.024981
1	2.219112	21	-0.043032	41	0.034913	61	-0.17094
2	3.023188	22	-0.021848	42	-0.024283	62	-0.032358
3	2.631353	23	0.067885	43	0.057423	63	-0.015907
4	2.134523	24	-0.108795	44	0.007494	64	0.002836
5	1.740770	25	0.034092	45	0.007490	65	-0.025769
6	1.163706	26	-0.021568	46	0.069468	66	0.014313
7	1.050706	27	-0.090079	47	-0.041651	67	-0.032372
8	0.731576	28	0.067005	48	0.053805	68	0.000539
9	0.529047	29	-0.097462	49	-0.033688	69	0.009454
10	0.565819	30	0.045899	50	-0.010172	70	-0.004264
11	0.269183	31	-0.004724	51	0.027343	71	0.020153
12	0.400907	32	-0.067016	52	-0.018481	72	-0.012862
13	0.258483	33	0.040531	53	0.050382	73	-0.006631
14	0.152469	34	-0.080065	54	0.013797	74	0.024158
15	0.281511	35	0.001872	55	-0.008711	75	-0.001513
16	0.062223	36	0.026506	56	0.033592	76	0.046734
17	0.126886	37	-0.092206	57	-0.035303	77	0.004383
18	0.160163	38	0.049849	58	0.018588	78	0.014859
19	-0.064121	39	-0.77489	59	-0.020023	79	-0.004000

and πF_o is the flux incident on the top of the atmosphere in the direction $(-\mu_o, \phi_o)$.

The decomposition of equation (A7) into Fourier components follows *Chandrasekhar* [1960, pp. 149-150]. The phase function times the single scattering albedo is expressed as a finite series of $L+1$ Legendre polynomials, P_l, where the coefficients ω_l are functions of τ, and $\dot{\omega}_0(\tau) = \omega(\tau)$.

$$\omega(\tau)P(\tau,\cos\theta) = \sum_{l=0}^{L}\omega_l(\tau)P_l(\cos\theta) \qquad (A9)$$

Using the addition theorem for spherical harmonics, this expression may be put in the form

$$\omega(\tau)P(\tau,\cos\theta) = \omega(\tau)P(\tau,\mu,\phi,\mu',\phi')$$

$$= \sum_{l=0}^{L}\omega_l(\tau)P_l(\mu)P_l(\mu')$$

$$+ 2\sum_{m=1}^{L}\sum_{l=m}^{L}\omega_l(\tau)Y_l^m(\mu)Y_l^m(\mu')\cos m(\phi-\phi') \qquad (A10)$$

where Y_l^m are the renormalized associated Legendre functions [*Dave and Armstrong*, 1970] and $Y_l^0 = P_l$. When the specific intensity is expanded similarly with respect to the solar azimuth angle ϕ_o,

$$I(\tau,\mu,\phi) = \sum_{m=0}^{L}I^m(\tau,\mu)\cos m(\phi-\phi_0) \qquad (A11)$$

we have the equation for the zeroth moment,

$$\mu\frac{dI^0(\tau,\mu)}{d\tau} = I^0(\tau,\mu) - \frac{1}{2}\sum_{l=0}^{L}\omega_l(\tau)P_l(\mu)\int_{-1}^{+1}P_l(\mu')I^0(\tau,\mu')d\mu'$$

$$- \frac{1}{4}F_o e^{-\tau/\mu_o}\sum_{l=0}^{L}\omega_l(\tau)P_l(\mu)P_l(-\mu_o) \qquad (A12)$$

and L additional independent equations, $m = 1$ to L, for components of the radiation field that are periodic in $(\phi-\phi_o)$.

$$\mu\frac{dI^m(\tau,\mu)}{d\tau} = I^m(\tau,\mu) - \frac{1}{2}\sum_{l=0}^{L}\omega_l(\tau)Y_l^m(\mu)\int_{-1}^{+1}Y_l^m(\mu')I^m(\tau,\mu')d\mu'$$

$$- \frac{1}{2}F_o e^{-\tau/\mu_o}\sum_{l=0}^{L}\omega_l(\tau)Y_l^m(\mu)Y_l^m(-\mu_o) \qquad (A13)$$

For this paper we are interested in the radiation field contributing to the photolysis rates,

$$J(\tau) = \pi F_o e^{-\tau/\mu_o} + 4\pi<I(\tau)> \qquad (A14)$$

where the mean intensity $<I>$ depends only on the zeroth order of the specific intensity,

$$<I(\tau)> = \frac{1}{4\pi}\int_0^{2\pi}d\phi\int_{-1}^{+1}d\mu\,I(\tau,\mu,\phi) = \frac{1}{2}\int_{-1}^{+1}d\mu\,I^0(\tau,\mu) \qquad (A15)$$

The method of solution for I^0 is described below (dropping the superscript zero notation). Solutions for higher orders of I are needed only if the azimuthal dependence of the radiation field is needed (e.g., to compare with observations) and can be performed in a similar manner.

The odd-even symmetry of the Legendre functions, $Y_l^m(-\mu) = (-1)^{l-m}Y_l^m(\mu)$, can be used to derive separate, but coupled equations for $j(\tau,\mu)$ and $h(\tau,\mu)$ defined as

$$j(\tau,\mu) = \frac{1}{2}[I(\tau,+\mu) + I(\tau,-\mu)] \qquad (A16)$$

$$h(\tau,\mu) = \frac{1}{2}[I(\tau,+\mu) - I(\tau,-\mu)] \qquad (A17)$$

with $0 < \mu < 1$. The integrals can be expressed in terms of j and h by noting that

$$\int_{-1}^{+1}I(\tau,\mu)P_l(\mu)d\mu = 2\int_0^1 j(\tau,\mu)P_l(\mu)d\mu \quad l\ \text{even} \qquad (A18)$$

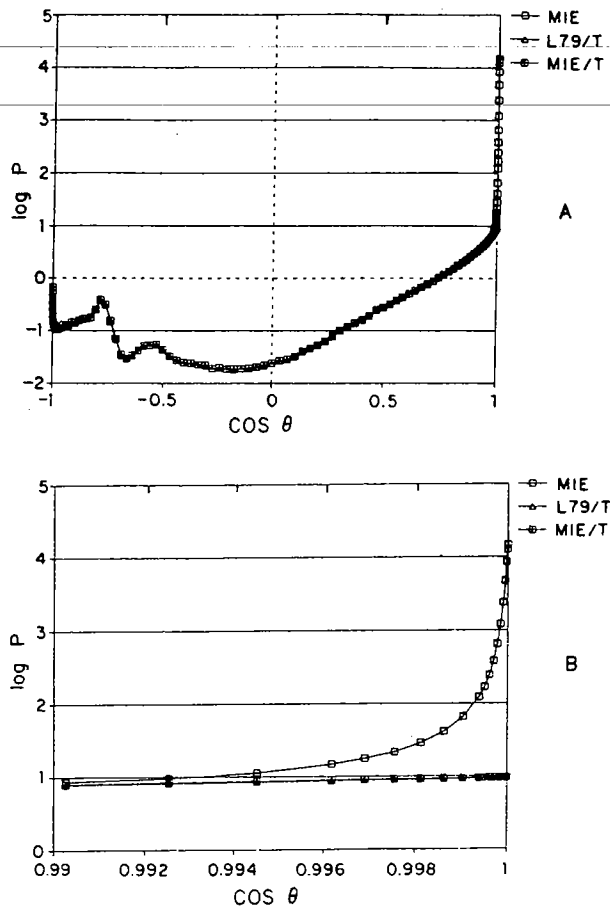$$\int_{-1}^{+1}I(\tau,\mu)P_l(\mu)d\mu = 2\int_0^1 h(\tau,\mu)P_l(\mu)d\mu \quad l\ \text{odd} \qquad (A19)$$

Fig. A3. Phase function for scattering of spheres of pure H_2O with a gamma distribution of effective radius 10 μm. The value of log P is plotted as a function of the cosine of the scattering angle. The Mie phase function at 400 nm (MIE) is compared to the truncated Mie phase function (MIE/T) and to the Legendre expansion of the truncated Mie phase function (L79/T). (*a*) The full scale. (*b*) An expanded scale about the forward peak.

Let Σ^{odd} denote the sum over all odd-numbered Legendre polynomials beginning with P_1, and Σ^{even} the sum over even polynomials beginning with P_0. Then we may derive a pair of coupled differential equations for j and h over the domain $0 < \mu < 1$.

$$\mu \frac{dj(\tau,\mu)}{d\tau} = \frac{1}{2}[(+\mu)\frac{dI(\tau,+\mu)}{d\tau} + (-\mu)\frac{dI(\tau,-\mu)}{d\tau}]$$

$$= h(\tau,\mu) - \Sigma^{\mathrm{odd}}\omega_l P_l(\mu)\int_0^1 P_l(\mu')h(\tau,\mu')d\mu'$$

$$- \frac{1}{2}F_o e^{-\tau/\mu_o}\Sigma^{\mathrm{odd}}\omega_l P_l(\mu)P_l(-\mu_o) \qquad (A20)$$

$$\mu \frac{dh(\tau,\mu)}{d\tau} = \frac{1}{2}[(+\mu)\frac{dI(\tau,+\mu)}{d\tau} - (-\mu)\frac{dI(\tau,-\mu)}{d\tau}]$$

$$= j(\tau,\mu) - \Sigma^{\mathrm{even}}\omega_l P_l(\mu)\int_0^1 P_l(\mu')j(\tau,\mu')d\mu'$$

$$- \frac{1}{2}F_o e^{-\tau/\mu_o}\Sigma^{\mathrm{even}}\omega_l P_l(\mu)P_l(-\mu_o) \qquad (A21)$$

We solve for $j(\tau,\mu)$ and $h(\tau,\mu)$ at a discrete set of angle points (μ_k, $k=1,K$) and over a discrete grid of optical depth (τ_i, $i=1,N$). The set of angle points are chosen to be the Gaussian quadrature points (μ_k) with associated weights (a_k) over the interval $0 < \mu < 1$. Then

the integrals over the cosine of the zenith angle in equations (A20) and (A21) are approximated by Gaussian quadrature, e.g.,

$$\int_0^1 P_l(\mu)j(\tau,\mu)d\mu = \sum_{k=1}^{K}a_k P_l(\mu_k)j(\tau,\mu_k) \qquad (A22)$$

For the Mie functions expanded to P_{79} we use $K = 40$, which is the minimum number of quadrature angles necessary for $L = 79$. For the τ grid, $\tau_1 = 0$ is chosen as the top of the atmosphere, and τ_N at the bottom of the atmosphere is the total optical depth. We use j_{ik} and h_{ik} to denote $j(\tau_i,\mu_k)$ and $h(\tau_i,\mu_k)$, respectively.

Regarding the coupled equations (A20) and A(21), note that the first derivative of j is a function only of h, and vice versa. For the case of isotropic or Rayleigh scattering [e.g., *Prather*, 1974] the odd terms Σ^{odd} vanish and the pair of equations (A20) and (A21) can be readily collapsed into a single second-order differential equation involving only j and $d^2 j/d\tau^2$. This second-order ordinary differential equation would be solved by using finite differences over a τ grid with second-order boundary conditions [*Auer*, 1967].

The innovative approach used here to solve the asymmetric scattering problem is to recognize that we can calculate j and $dh/d\tau$ at odd grid points, and h and $dj/d\tau$ at the alternating even grid points. Requiring N to be odd, there are N-2 equations of the following type for each interior grid point,

$$k=1,K$$

$$[\frac{dj}{d\tau}]_{2k} = \frac{j_{3k}-j_{1k}}{\tau_{3k}-\tau_{1k}} \qquad (A23)$$

$$[\frac{dh}{d\tau}]_{3k} = \frac{h_{4k}-h_{2k}}{\tau_{4k}-\tau_{2k}} \qquad (A24)$$

where $[dj/d\tau]_{2k}$ is equated to a linear combination of $h_{2k'}$ ($k' = 1,K$) and $[dh/d\tau]_{3k}$, to a linear combination of $j_{3k'}$. For the boundary conditions we need two equations coupling j at the boundary with h at the adjacent interior point. At the upper boundary a first-order Taylor expansion is applied

$$h_{2k} = h_{1k} + [\frac{dh}{d\tau}]_{1k}(\tau_2-\tau_1) + \text{second-order terms} \qquad (A25)$$

The first derivative in equation (A25) is expressed as a linear combination of $j_{1k'}$ using equation (A21), and we substitute $j_{1k} = h_{1k}$ because there is no diffuse radiation incident on the top of the atmosphere (i.e., $I(\tau=0,-\mu) = 0$). At the lower boundary a similar expansion is used,
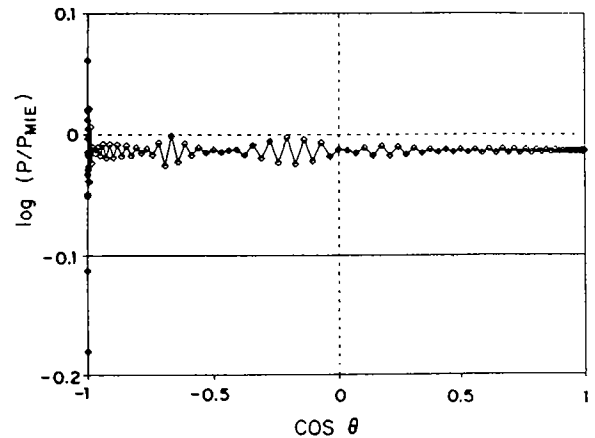

Fig. A4. Comparison of the Legendre expansion at 400 nm (P) to the truncated Mie phase function (P_{MIE}). The logarithm of the ratio is plotted as a function of the cosine of the scattering angle.
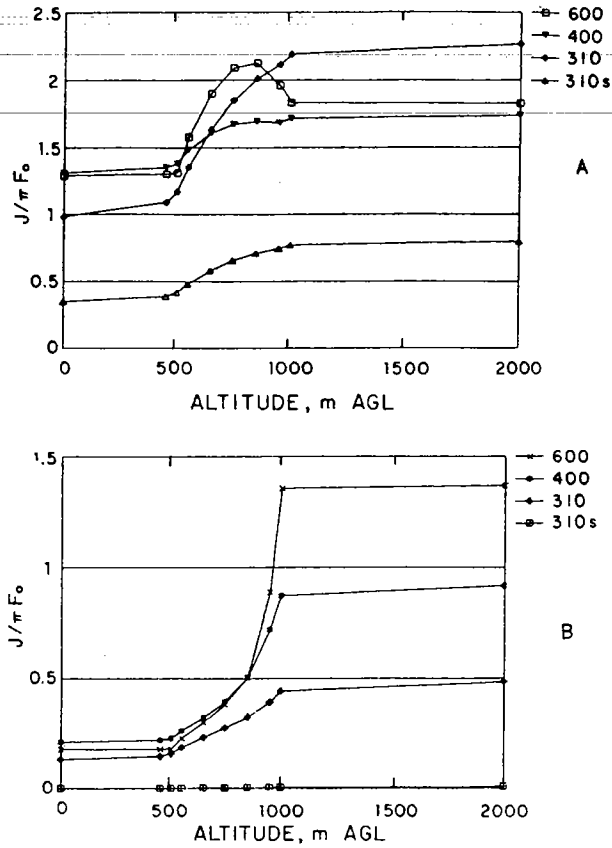
Fig. A5. Monochromatic J values normalized to the reference value πF_o, as a function of altitude. A cloud of renormalized optical thickness $\tau_{ex}^* = 4$ is embedded between altitudes 500 m and 1000 m. The ground reflectivity is 0.1. Results are shown for three different wavelengths (310, 400, and 600 nm) and two solar zenith angles, (a) $\mu_o = 1$ and (b) $\mu_o = 0.25$. Results at 310 nm are shown both with and without absorption from stratospheric ozone (plots 310s and 310, respectively).

$$h_{N-1,k} = h_{Nk} - [\frac{dh}{d\tau}]_{Nk}(\tau_N - \tau_{N-1}) + \text{second-order terms} \qquad (A26)$$

but the relationship between h_{Nk} and j_{Nk} is more complex. The lower boundary is assumed to be Lambertian, that is, the specific intensity reflected from the surface is isotropic ($I(\tau_N, +\mu) = I_N^+$) with a hemispheric flux equal to a fraction (λ) of the flux incident on the lower boundary. The equations are

$$h_{Nk} = I_N^+ - j_{Nk} \qquad (A27)$$

and

$$I_N^+ = \frac{4\lambda}{1+\lambda} \int_0^{+1} j_N(\mu)\mu d\mu = \frac{4\lambda}{1+\lambda} \sum_{k=1}^{K} j_{Nk}\mu_k a_k \qquad (A28)$$

(An alternate lower boundary condition may be applied in an optically thick atmosphere for which the radiation field can be considered symmetric in μ: $h_{Nk} = 0$.) For the higher-order moments of the radiation field (I_m, $m=1,L$) a Lambertian surface is black, $\lambda = 0$.

The $NK \times NK$ system of linear equations is efficiently solved as a block tri-digonal system of equations with $K \times K$ blocks [Feautrier, 1964]. Results from the forward pass through the system can be saved and used to recompute the solution for a different right-hand side at negligible increase in computation (i.e., different solar zen-
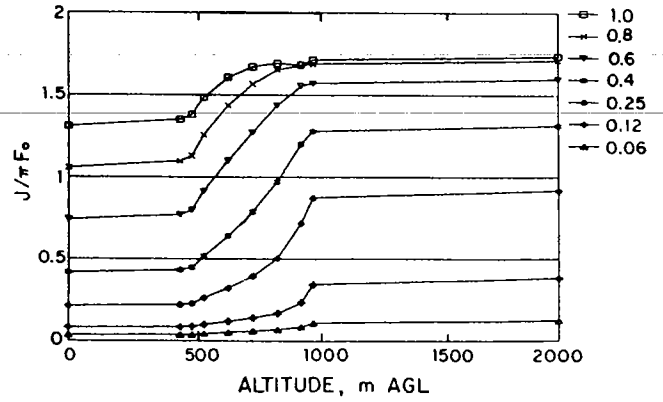

Fig. A6. Monochromatic J values at 400 nm normalized to the reference value πF_o, as a function of altitude. A cloud of renormalized optical thickness $\tau_{ex}^* = 2$ is embedded between altitudes 500 m and 1000 m. The ground reflectivity is 0.1. Results are shown for seven values of the zenith angle, ranging from $\mu_o = 0.06$ to $\mu_o = 1$.

ith angles). The right-hand side involves only terms proportional to F_o and the entire solution is, of course, linear in F_o. An obvious consequence of this linearity is that the average scattered intensity over a day can be derived with a single calculation by first averaging the source term, including the angular dependence in terms such as $P(\mu)P(-\mu_o)$. The computational time on an IBM 4381-13 is 49 seconds for the cases shown here (only I_o, $K = 40$, $N = 123$) including 7 different solar zenith angles.

A 5. The Radiation Field with a Stratus Cloud

The above solutions have been applied to a stratuslike cloud in the boundary layer. The monochromatic J values, defined as $J/\pi F_o$ from equation (A14), are shown as a function of altitude for a variety of conditions in Figures A5-A9. The optical properties have been described above, and the calculations embed the cloud between altitudes 500 m and 1000 m in a Rayleigh scattering medium. The optical properties of the cloud are taken from the Mie calculations at 400 nm for all three wavelengths: 310, 400 and 600 nm.
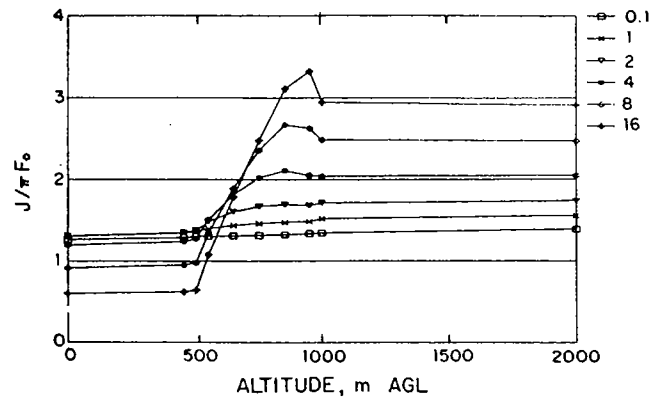

Fig. A7. Monochromatic J values at 400 nm normalized to the reference value πF_o, as a function of altitude. A cloud of renormalized optical thickness τ_{ex}^* is embedded between altitudes 500 m and 1000 m. The ground reflectivity is 0.1, and $\mu_o = 1$. Results are shown for six values of τ_{ex}^* ranging from 0.1 to 16.

TABLE A3. J values in a Cloudy Atmosphere

Altitude m	cos (solar zenith angle)
	1.00	0.80	0.60	0.40	0.25	0.12	0.06
At 310 nm
top	1.044	1.030	1.016	1.005	1.000	1.000	1.000
12,000	0.750	0.548	0.321	0.111	0.017	0.000	0.000
7,000	0.760	0.539	0.299	0.093	0.012	0.000	0.000
4,000	0.732	0.507	0.270	0.077	0.009	0.000	0.000
2,000	0.679	0.462	0.238	0.064	0.007	0.000	0.000
1,000	0.644	0.436	0.223	0.059	0.006	0.000	0.000
900	0.622	0.423	0.215	0.055	0.006	0.000	0.000
800	0.596	0.400	0.196	0.048	0.005	0.000	0.000
700	0.568	0.371	0.175	0.041	0.004	0.000	0.000
600	0.532	0.337	0.154	0.036	0.004	0.000	0.000
500	0.485	0.297	0.132	0.030	0.003	0.000	0.000
400	0.454	0.272	0.119	0.027	0.003	0.000	0.000
0	0.386	0.227	0.098	0.023	0.002	0.000	0.000
At 400 nm
top	1.666	1.671	1.637	1.540	1.407	1.238	1.138
12,000	1.748	1.747	1.689	1.528	1.290	0.894	0.525
7,000	1.769	1.758	1.676	1.464	1.151	0.649	0.271
4,000	1.764	1.744	1.643	1.390	1.025	0.487	0.169
2,000	1.737	1.712	1.598	1.316	0.918	0.381	0.124
1,000	1.716	1.690	1.572	1.281	0.873	0.343	0.111
900	1.691	1.676	1.507	1.084	0.593	0.192	0.079
800	1.690	1.618	1.358	0.874	0.441	0.155	0.067
700	1.648	1.508	1.188	0.712	0.356	0.131	0.058
600	1.556	1.355	1.010	0.581	0.293	0.111	0.049
500	1.381	1.130	0.797	0.447	0.228	0.089	0.039
400	1.352	1.099	0.771	0.432	0.221	0.086	0.038
0	1.310	1.058	0.740	0.414	0.212	0.082	0.037

J values are normalized to the solar flux. The cloud is located between 500 and 1000 m, with renormalized optical thickness of 2, single scattering albedo of 1, surface reflectivity (Lambertian) of 0.1, and absorption by stratospheric ozone with optical depth 1 at 310 nm.

Figure A5 compares the J values as a function of wavelength for two solar zenith angles, μ_o = 1 and 0.25. Major differences with wavelength are due to the amount of Rayleigh scattering above the cloud and to the inclusion of stratospheric ozone absorp-

ALTITUDE, m AGL

Fig. A8. Monochromatic J values at 310 nm normalized to the reference value πF_o, as a function of altitude. A cloud of renormalized optical thickness τ_{ex}^* is embedded between altitudes 500 m and 1000 m. The ground reflectivity is 0.1, and μ_o = 0.6. Absorption by stratospheric ozone is not included. Results are shown for five values of τ_{ex}^* ranging from 0.1 to 16.

tion at 310 nm. (Ozone absorption at 600 nm by the Chappuis bands, $\tau \sim 0.04$, would be negligible except at very small solar zenith angles and is not included.) All wavelengths show enhancements within and above the cloud. At 600 nm the atmosphere is almost transparent, and the J value maximizes within the cloud. The pair of calculations at 310 nm shows that stratospheric absorption tends to scale the results by e^{-1/μ_o}.

Figure A6 shows how the J values depend on solar zenith angle for the standard cloud case at 400 nm. The J value above the cloud changes only slowly with zenith angle for μ_o > 0.5, but the radiation field in the bottom half of the cloud and near the ground decreases rapidly, almost linearly, with μ_o.

Figure A7 demonstrates the dependence of J values on the optical depth of the cloud at 400 nm for μ_o = 1. As the optical thickness of the cloud increases above 1, the J value in the top half of the cloud increases almost logarithmically with optical depth, while that in the lower half decreases by about the same proportion. Similar calculations at 310 nm for μ_o = 0.6, and with no absorption from stratospheric ozone, are shown in Figure A8. The basic response to solar zenith angle is similar to Figure A7.

Figure A9 takes the case from Figure A8 with optical depth equal to 4 and compares with three special cases. An increase in the ground reflectivity from 0.1 to 0.3 leads to a 40% increase in J values at the lower boundary of the cloud, but only a 6% increase at the top. A reduction in the single scattering albedo from 1 to
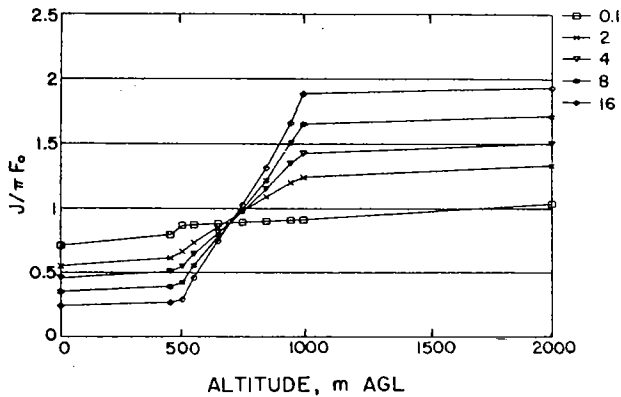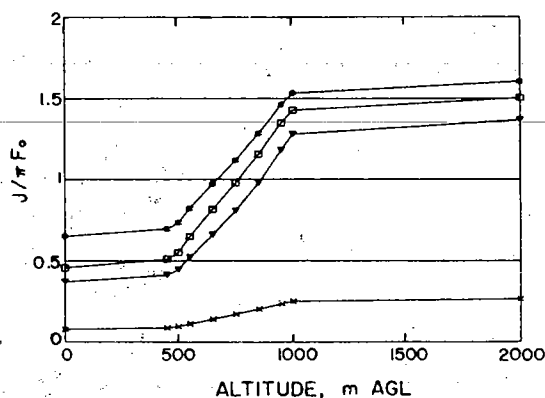
Fig. A9. Monochromatic J values at 310 nm normalized to the reference value πF_0, as a function of altitude. A cloud of renormalized optical thickness $\tau_{ex}^* = 4$ is embedded between altitudes 500 m and 1000 m. In the standard case (squares) the ground reflectivity is 0.1, $\mu_0 = 0.6$, the single scattering albedo is 1, and no absorption by stratospheric ozone is included. Results are shown for the effects of increased ground reflectivity from 0.1 to 0.3 (number signs), decreased single scattering albedo from 1 to 0.98 (inverted triangles), and absorption by stratospheric ozone (crosses).

0.98 results in about 10-20% reduction to the J values increasing from top to bottom of the cloud. Including the absorption by stratospheric ozone greatly reduces the J values, by almost a uniform scaling factor of $0.18 \sim e^{-1/\mu_0}$.

Results from the two standard cases used in the photochemical model are given in Table A3. These tables give monochromatic J values, $J/\pi F_0$, throughout the troposphere as a function of altitude and cosine of the solar zenith angle. Rayleigh scattering is included as outlined in Table A1 and the ground reflectivity is assumed to be 0.1 (Lambertian). Ozone absorption is included at 310 nm and determines the strong falloff with zenith angle at this wavelength.

REFERENCES

Aerovironment, Inc., AVKERN application report, Rep. AV-FR-83/501R2, Pasadena, Calif., 1984.

Atkinson, R., and A. L. Lloyd, Evaluation of kinetic and mechanistic data for modeling of photochemical smog, *J. Phys. Chem. Ref. Data, 13,* 315-444, 1984.

Auer, L., Improved boundary conditions for the Feautrier method, *Astrophys. J., 150,* 153-155, 1967.

Betterton, E. A., and M. R. Hoffmann, Kinetics, mechanism and thermodynamics of the reversible reaction of methylglyoxal (CH_3COCHO) with S(IV), *J. Phys. Chem., 91,* 3011-3020, 1987.

Betterton, E. A., and M. R. Hoffmann, Henry's law constants of some environmentally important aldehydes, *Environ. Sci. Technol., 22,* 1415-1418, 1988a.

Betterton, E. A., and M. R. Hoffmann, Oxidation of aqueous SO_2 by peroxymonosulfate, *J. Phys. Chem., 92,* 5962-5965, 1988b.

Bielski, B. H. J., D. E. Cabelli, R. L. Arudi, and A. B. Ross, Reactivity of HO_2/O_2^- radicals in aqueous solution, *J. Phys. Chem. Ref. Data, 14,* 1041-1100, 1985.

Cabelli, D. E., and B. H. J. Bielski, Pulse radiolysis study of the kinetics and mechanisms of the reactions between manganese(II) complexes and HO_2/O_2^- radicals, 2, The phosphate complex and an overview, *J. Phys. Chem., 88,* 6291-6294, 1984.

Caughey, S. J., B. A. Crease, and W. T. Roach, A field study of nocturnal stratocumulus. II. Turbulence structure and entrainment, *Q. J. R. Meteorol. Soc., 108,* 125-144, 1982.

Chameides, W. L., The photochemistry of a remote marine stratiform cloud, *J. Geophys. Res., 89,* 4739-4755, 1984.

Chameides, W. L., and D. D. Davis, The free radical chemistry of cloud droplets and its impact upon the composition of rain, *J. Geophys. Res., 87,* 4863-4877, 1982.

Chandrasekhar, S., *Radiative Transfer,* 393 pp., Dover, New York, 1960.

Chang, J. S., R. A. Brost, I. S. A. Isaksen, S. Madronich, P. Middleton, W. R. Stockwell, and C. J. Walcek, A three-dimensional Eulerian acid deposition model. Physical concepts and formulation, *J. Geophys. Res., 92,* 14681-14700, 1987.

Cochran, W. D., and L. M. Trafton, Raman scattering in the atmospheres of the major planets, *Astrophys. J., 219,* 756-762, 1978.

Conklin, M. H., and M. R. Hoffmann, Metal ion - S(IV) chemistry III. Thermodynamics and kinetics of transient iron(III)-sulfur(IV) complexes, *Environ. Sci. Technol., 22,* 899-907, 1988a.

Conklin, M. H., and M. R. Hoffmann, Metal ion - S(IV) chemistry II. Kinetic studies of the redox chemistry of copper(II)-sulfur(IV) complexes, *Environ. Sci. Technol., 22,* 891-898, 1988b.

Conocchioli, T. J., E. J. Hamilton, Jr., and N. Sutin, The formation of iron (IV) in the oxidation of iron (II), *J. Am. Chem. Soc., 87,* 926-927, 1965.

Daum, P. H., S. E. Schwartz, and L. Newman, Acidic and related constituents in liquid water stratiform clouds, *J. Geophys. Res., 89,* 1447-1458, 1984.

Dave, J. V., and B. H. Armstrong, Computation of high-order associated Legendre polynomials, *J. Quart. Spectros. Radiat. Transfer, 10,* 557-562, 1970.

Davies, G., Some aspects of the chemistry of manganese(III) in aqueous solution, *Coord. Chem. Rev., 4,* 199-224, 1969.

Deirmendjian, D., *Electromagnetic Scattering on Spherical Polydispersions,* 287 pp., American Elsevier, New York, 1969.

Duckworth, S., and D. Crowe, Sulfur dioxide and sulfate trends, Bakersfield, 1977-1978 report. Tech. Serv. Div., Calif. Air Resour. Board, Sacramento, 1979.

Environmental Protection Agency, Development of the 1980 NAPAP emissions inventory, Rep. EPA/600/7-86/057a, Research Triangle Park, N.C., 1986.

Farhataziz, and A. B. Ross, Selected specific rates of transients from water in aqueous solution, III.,Hydroxyl radical and perhydroxyl radical and their radical ions, Rep. NSRDBS-NBS 59, U.S. Dep. of Commerce, Washington, D.C., 1977.

Faust, B. C., Photo-induced reductive dissolution of hematite (α-Fe_2O_3) by S(IV) oxyanions, Ph.D. thesis, Calif. Inst. of Technol., Pasadena, 1985.

Feautrier, P., Sur la resolution numerique de l'equation de transfert, *C. R. Acad. Sci. Paris, 258,* 3189-3191, 1964.

Flynn, C. M., Jr., Hydrolysis of inorganic iron(III) salts, *Chem. Rev., 84,* 31-41, 1984.

Gershenzon, Y. M., A. V. Ivanov, S. I. Kucheryavyi, and V. B. Rozenshtein, Annihilation of OH radicals on the surfaces of substances chemically similar to atmospheric aerosol particles of the Earth's atmosphere, *Kinet. Katal., 27,* 1069-1074, 1986.

Gervat, G. P., P. A. Clark, A. R. W. Marsh, I. Teasdale, A. S. Chandler, T. W. Choularton, M. J. Gay, M. K. Hill, and T. A. Hill, Field evidence for the oxidation of SO_2 by H_2O_2 in cap clouds, *Nature, 333,* 241-243, 1988.